01 Jun 2002

Differential Cross Sections and Cross-Section Ratios for the Electron-Impact Excitation of the Neon $2p^5 3s$ Configuration

Murtadha A. Khakoo

James M. Wrkich

Mary Lu Larsen

G. Kleiban

et. al. For a complete list of authors, see https://scholarsmine.mst.edu/phys_facwork/1510

Recommended Citation

M. A. Khakoo and J. M. Wrkich and M. L. Larsen and G. Kleiban and I. Kanik and S. Trajmar and M. J. Brunger and P. J. Teubner and A. Crowe and C. J. Fontes and R. E. Clark and V. Zeman and K. Bartschat and D. H. Madison and R. C. Srivastava and A. D. Stauffer, "Differential Cross Sections and Cross-Section Ratios for the Electron-Impact Excitation of the Neon $2p^5 3s$ Configuration," *Physical Review A - Atomic, Molecular, and Optical Physics*, vol. 65, Institute of Physics - IOP Publishing, Jun 2002.
The definitive version is available at https://doi.org/10.1103/PhysRevA.65.062711

PHYSICAL REVIEW A, VOLUME 65, 062711

Differential cross sections and cross-section ratios for the electron-impact excitation of the neon $2p^5 3s$ configuration

M. A. Khakoo,[1] J. Wrkich,[1] M. Larsen,[1,*] G. Kleiban,[1] I. Kanik,[2] S. Trajmar,[2] M. J. Brunger,[3] P. J. O. Teubner,[3]
A. Crowe,[4] C. J. Fontes,[5] R. E. H. Clark,[6] V. Zeman,[7] K. Bartschat,[8] D. H. Madison,[9] R. Srivastava,[10] and A. D. Stauffer[11]
[1]*Department of Physics, California State University, Fullerton, California 92834*
[2]*Jet Propulsion Laboratory, California Institute of Technology, Pasadena, California 91109*
[3]*Flinders University of South Australia, GPO Box 2100, Adelaide, S.A. 5001, Australia*
[4]*Department of Physics, University of Newcastle-upon-Tyne, Newcastle, NE1 7RU, United Kingdom*
[5]*Applied Theoretical and Computational Physics Division, Los Alamos National Laboratory, Los Alamos, New Mexico 87544*
[6]*International Atomic Agency, Atomic and Molecular Data Unit, Vienna A-1400, Austria*
[7]*Chemical Physics Theory Group, University of Toronto, Toronto, Canada M5S 3H6*
[8]*Department of Physics & Astronomy, Drake University, Des Moines, Iowa 50311*
[9]*Department of Physics, University of Missouri, Rolla, Missouri 65401*
[10]*Department of Physics, Indian Institute of Technology Roorkee, Rourkee-247667, India*
[11]*Department of Physics and Astronomy, York University, Toronto, Canada M3J 1P3*

(Received 17 December 2001; revised manuscript received 4 March 2002; published 7 June 2002)

Electron-impact differential cross-section measurements for the excitation of the $2p^5 3s$ configuration of Ne are reported. The Ne cross sections are obtained using experimental differential cross sections for the electron-impact excitation of the $n=2$ levels of atomic hydrogen [Khakoo *et al.*, Phys. Rev. A **61**, 012701-1 (1999)], and existing experimental helium differential cross-section measurements, as calibration standards. These calibration measurements were made using the method of gas mixtures (Ne and H followed by Ne and He), in which the gas beam profiles of the mixed gases are found to be the same within our experimental errors. We also present results from calculations of these differential cross sections using the *R*-matrix and unitarized first-order many-body theory, the distorted-wave Born approximation, and relativistic distorted-wave methods. Comparison with available experimental differential cross sections and differential cross-section ratios is also presented.

DOI: 10.1103/PhysRevA.65.062711 PACS number(s): 34.80.Dp

I. INTRODUCTION

Electron-impact excitation of the ground np^6 state of heavy noble gases to the first excited-electron $np^5(n+1)s$ configuration has been shown to provide a unique system where both differential cross sections (DCS's) and their ratios provide valuable insights on relativistic interactions which control the electron scattering dynamics [1]. The aim of this investigation is to provide both reliable experimental differential cross sections and differential cross-section ratios (r,r',r'') [1] for the excitation of Ne from its $2p^6$ ground state configuration to the first-excited $2p^5 3s$ configuration and a detailed comparison with available theoretical models. The $2p^5 3s$ configuration is made up of the four levels, listed with increasing energy above the ground state: $(2p^5 3s)\times[3/2]^\circ_2$, $(2p^5 3s)[3/2]^\circ_1$, $(2p^5 3s)[1/2]^\circ_0$ and $(2p^5 3s)\times[1/2]^\circ_1$, following the $[jK]_J$ coupling scheme [2].[1] We have investigated similar systems in Kr $(4p^6 \rightarrow 4p^5 5s)$ [3] and Xe $(5p^6 \rightarrow 5p^5 6s)$ [4] previously, but agreement between the experiment and theoretical models was found to be qualitative at best. Indeed in several cases, large disagreements were observed between experiment and theory. Those discrepancies were clearly due to the difficulty of the theoretical models in handling relativistic effects in the dynamics of the scattering, as well as in the structure calculation of these heavy rare-gas targets. The current work in Ne was carried out to provide DCS's and DCS ratios for the lightest member of this family, and present the opportunity for electron scattering theory to see if it can obtain better agreement with the experiment due to the reduced target relativistic effects.

Previous measurements in Ne, using conventional energy-loss spectroscopy, were carried out by Nicholl and Mohr [5] for the $(2p^5 3s)[1/2]^\circ_1$ level. Following this Tam and Brion [6] and Roy and Carette [7] measured relative DCS's for the individual $2p^5 3s$ levels. Thereafter, the DCS measurements of Register *et al.* [8] provide the only results of absolute DCS's for excitation of the individual levels which make up the $2p^5 3s$ configuration, to date. These latter measurements were taken at incident energies (E_0) of 25, 30, 50, and 100 eV and for scattering angles (θ) from 5° to 140°.

Additionally, McConkey and co-workers [9], have measured polarization-correlation parameters for excitation of the $(2p^5 3s)[1/2]^\circ_1$ level from the ground state level using an electron-photon coincidence method. Due to the reduced signal levels in coincidence measurements, their data were restricted to $E_0=40$ eV and 50 eV and $\theta=5°$ to 45°. Reasonable agreement with theory [distorted-wave approximation

---

*Present address: Department of Physics, University of Wisconsin, Madison, WI 53706.

[1] The core's total angular momentum quantum number $=j$; $K=j+l_2$, where $l_2=0$ is the electron orbital angular momentum quantum number for the excited $3s$ orbital; thus $K=j$.

[10] (DWBA) and first-order many-body theory [11] (FOMBT)] for P_1, P_2, and P_3 polarization parameters was observed at these small angles. From this result and from observation of the P_4 polarization [9], it was inferred that Ne essentially displayed *LS*-coupled behavior. The (linear) polarization of emitted radiation excited by spin-polarized electrons incident on Ne, was measured by Zeman *et al.* [12]. These measurements were found to be in qualitative agreement, at best, when compared with the semirelativistic *R*-matrix model of Berrington *et al.* [13]. The sublevel excitation of metastable Ne $(2p^5 3s)[3/2]^\circ_2$ from the ground state by electrons was made by Fisher *et al.* [14]. They probed the polarization of the excited metastable atoms using laser-induced fluorescence of the system: $(2p^5 3s)[3/2]^\circ_2 \rightarrow (2p^5 3p)[3/2]_1 \rightarrow (2p^5 3s)[1/2]^\circ_0$. The measurements were used to obtain the alignment of the $(2p^5 3s)[3/2]^\circ_2$ level by applying an *LS*-coupling scheme to extrapolate back to the alignment of this level. Their results were compared to the *R*-matrix [15] and relativistic distorted-wave approximation (RDWA) [16] calculations. However, the effect of cascade in these measurements could not be accounted for, thus restricting any reasonable comparison with theory. Recently, Kanik *et al.* [17] measured vacuum UV emission cross sections for the $(2p^6)^1S \rightarrow (2p^5 3s)[3/2]^\circ_1$, $(2p^5 3s)[1/2]^\circ_1$ electron-impact excitations at 73.6 nm and 74.4 nm, from threshold to 400 eV impact energies. These emission cross sections have large uncertainties, viz. absolute ±41% and relative ±22.2%; these measurements are also not cascade corrected. There also exist the unpublished, absolute DCS's for the electron impact excitation of the $2p^6$ summed levels of Ne of Brunger [18] at E_0 of 20, 30, and 40 eV for θ from 5° to 90°.

The use of DCS ratios as an alternative set of parameters for probing scattering behavior has been recently highlighted for the heavy rare gases (Bartschat and Madison [19], Khakoo *et al.* [1], and Guo *et al.* [3,20]). These DCS ratios can be determined more accurately and readily than DCS's or coherence parameters, and provide additional tests of theoretical models [3]. DCS ratios σ for the various levels of Ne are defined as follows:

$$r=\frac{\sigma(3s[3/2]_2)}{\sigma(3s'[1/2]_0)},\quad r'=\frac{\sigma(3s[3/2]_1)}{\sigma(3s'[1/2]_1)},$$

$$r''=\frac{\sigma(3s[3/2]_2)}{\sigma(3s'[3/2]_1)}. \tag{1}$$

In the single-configuration representation, the $2p^5 3s$ levels in Ne can be expressed in the intermediate-coupling scheme [2] in terms of *LS*-coupling wave functions $|\phi\rangle$ as

$$|3s[3/2]_2\rangle=|3\,^3P_2\rangle,$$

$$|3s[3/2]_1\rangle=\alpha|3\,^3P_1\rangle+\beta|3\,^1P_1\rangle,$$

$$|3s'[1/2]_0\rangle=|3\,^3P_0\rangle,$$

$$|3s'[1/2]_1\rangle=\alpha|3\,^1P_1\rangle-\beta|3\,^3P_1\rangle. \tag{2}$$

Here α and β are the intermediate-coupling (unitary) mixing coefficients. Note we have chosen to present the results in the $(LS)_J$ phase convention. Hence, there are some sign changes with respect to the coefficients given by Bartschat and Grum-Grzhimailo [21], but the only important aspect is, of course, a consistent treatment in either one of these phase conventions. Note that a $(SL)_J$ phase convention will have different relative signs for the α, β coefficients as compared to the $(LS)_J$ phase convention. The values of (α, β) based on the Cowan code (11-configuration model) used by the unitarized first-order many-body theory (UFOMBT) and the CIV3 code used by the *R*-matrix calculation are (0.940, 0.340) and (0.985, 0.175), respectively. Mixing coefficients associated with additional configurations were at least an order of magnitude smaller than α and β. The Cowan code mixing coefficients (amplitudes) for Ne are displayed in Table I.

From Eqs. (1) and (2), we see that r considers excitation to optically forbidden levels excitable essentially via spin-exchange. In the limiting case of degenerate fine-structure levels [19], r attains its *LS*-coupling limit of 5, i.e., *the statistical weight ratio of the respective* ($J=2$ and $J=0$) *levels*. The ratio r' considers excitations to the optically allowed $J=1$ levels. However, these $J=1$ levels have mixed triplet-singlet character. In the optical limit (high E_0 and small θ), application of dipole selection rules show, within this single-configuration coupling scheme, a limit for r':

$$\text{dipole lim } r'=\beta^2/\alpha^2. \tag{3}$$

Deviation from the optical limit could indicate either the importance of the triplet part of the $J=1$ components or the need for additional configuration singlet levels in the model to describe these mixed levels. On the other hand, if only pure spin-exchange excitation of these levels occurs, only the $|^3P\rangle$ *LS* component in Eq. (2) is excited, and now

$$\text{exchange lim } r'=\alpha^2/\beta^2. \tag{4}$$

A third parameter r'' provides additional information on the coupling scheme needed to describe the metastable, optically forbidden levels *relative* to the optically allowed levels, and consequently completes the framework of these ratios. Ratio measurements not only provide accurate values for comparison with theoretical models, but also tests of the target wave functions used in these models as well as the treatment of scattering dynamics (projectile electron-target interactions) [1].

In this paper we present high resolution DCS measurements for the $(2p^6)[0]_0 \rightarrow (2p^5 3s)[3/2]^\circ_2$, $(2p^5 3s)\times[3/2]^\circ_1$, $(2p^5 3s)[1/2]^\circ_0$ and $(2p^5 3s)[1/2]^\circ_1$ electron impact excitation. The present measurements are taken at E_0 values of 20, 30, 40, 50, and 100 eV over the range of θ from 1° to 130°. We also present Brunger's unpublished experimental DCS's [18] for the summed $2p^5\,3s$ levels and we additionally report semirelativistic 31-state *R*-matrix, UFOMBT, DWBA, and RDWA calculations, which are compared

TABLE I. Mixing coefficients for the $2p^5 3s$ configuration of Ne taken from the Cowan code. Four configurations are used here. Numbers in square brackets indicate negative powers of ten.

State	Amplitude	Core	Valence	LS Term
$(2p^5 3s)/[3/2]^{\circ}_2$	9.998600 [01]	$(..2p^5)^2P$	$(3s^1)^2S$	3^3P
	-1.701550 [10]	$(..2p^5)^2P$	$(3d^1)^2D$	3^3F
	1.059900 [04]	$(..2p^5)^2P$	$(3d^1)^2D$	3^3D
	-1.016500 [02]	$(..2p^5)^2P$	$(3d^1)^2D$	3^3P
	-8.652900 [05]	$(..2p^5)^2P$	$(3d^1)^2D$	3^1D
	5.691900 [03]	$(..2p^5)^2P$	$(4s^1)^2S$	4^3P
	2.738000 [03]	$(..2p^5)^2P$	$(5s^1)^2S$	5^3P
	-1.164600 [02]	$(..2s^1 2p^6)^2S$	$(3p^1)^2P$	6^3P
$(2p^5 3s)[3/2]^{\circ}_1$	9.401700 [01]	$(..2p^5)^2P$	$(3s^1)^2S$	3^3P
	3.402700 [01]	$(..2p^5)^2P$	$(3s^1)^2S$	3^1P
	1.057800 [04]	$(..2p^5)^2P$	$(3d^1)^2D$	3^3D
	-9.760500 [03]	$(..2p^5)^2P$	$(3d^1)^2D$	3^3P
	-2.595300 [03]	$(..2p^5)^2P$	$(3d^1)^2D$	3^1P
	5.248600 [03]	$(..2p^5)^2P$	$(4s^1)^2S$	4^3P
	-5.314500 [03]	$(..2p^5)^2P$	$(4s^1)^2S$	4^1P
	2.535600 [03]	$(..2p^5)^2P$	$(5s^1)^2S$	5^3P
	-2.572600 [03]	$(..2p^5)^2P$	$(5s^1)^2S$	5^1P
	-1.096800 [02]	$(..2s^1 2p^6)^2S$	$(3p^1)^2P$	6^3P
	-3.119000 [03]	$(..2s^1 2p^6)^2S$	$(3p^1)^2P$	6^1P
$(2p^5 3s)[1/2]^{\circ}_0$	9.998600 [01]	$(..2p^5)^2P$	$(3s^1)^2S$	3^3P
	-1.059500 [02]	$(..2p^5)^2P$	$(3d^1)^2D$	3^3P
	5.693000 [03]	$(..2p^5)^2P$	$(4s^1)^2S$	4^3P
	2.738600 [03]	$(..2p^5)^2P$	$(5s^1)^2S$	5^3P
	-1.168400 [02]	$(..2s^1 2p^6)^2S$	$(3p^1)^2P$	6^3P
$(2p^5 3s)[1/2]^{\circ}_1$	-3.402900 [01]	$(..2p^5)^2P$	$(3s^1)^2S$	3^3P
	9.400700 [01]	$(..2p^5)^2P$	$(3s^1)^2S$	3^1P
	5.838300 [05]	$(..2p^5)^2P$	$(3d^1)^2D$	3^3D
	3.742000 [03]	$(..2p^5)^2P$	$(3d^1)^2D$	3^3P
	-7.678600 [03]	$(..2p^5)^2P$	$(3d^1)^2D$	3^1P
	-2.252800 [03]	$(..2p^5)^2P$	$(4s^1)^2S$	4^3P
	-1.561800 [02]	$(..2p^5)^2P$	$(4s^1)^2S$	4^1P
	-1.048500 [03]	$(..2p^5)^2P$	$(5s^1)^2S$	5^3P
	-7.454000 [03]	$(..2p^5)^2P$	$(5s^1)^2S$	5^1P
	3.989700 [03]	$(..2s^1 2p^6)^2S$	$(3p^1)^2P$	3^3P
	-8.656300 [03]	$(..2s^1 2p^6)^2S$	$(3p^1)^2P$	3^1P

with the experimental measurements. For the DWBA, separate calculations were made using two sets of wave functions. These are the 15-state wave functions from the CIV3 code used in the *R*-matrix (CIV3-15-DWBA) and Hartree-Fock (HF-DWBA) wave functions. For the RDWA two separate calculations using a single configuration (SCGS-RDWA) and a multiconfiguration ground state (MCGS-RDWA) were also carried out.

II. EXPERIMENT

Two instruments were used in this work. Both setups have been discussed previously, so only a brief summary will be given here.

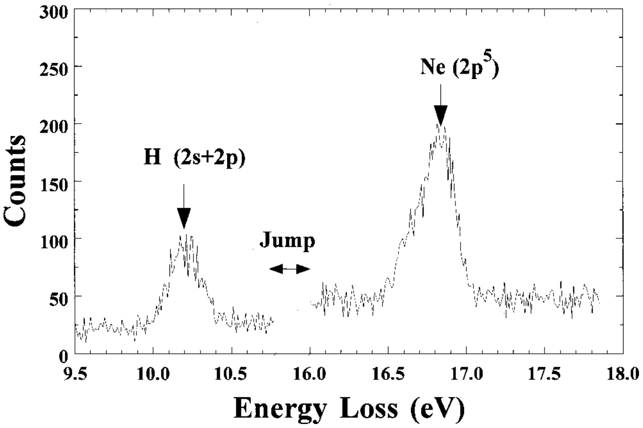

FIG. 1. Electron energy-loss spectrum of a mixture of Ne, H, and H_2 taken with the discharge on condition, showing the H($n=2$) and the Ne($n=3$) features. The E_0 and θ values are 100 eV and 80°, respectively. See text for discussion.

A. Low energy-resolution experiment

1. Experimental procedures

In the first instrument which was described in more detail in [22], the atomic beam was generated by a capillary needle and crossed a monochromatic beam of electrons of incident energy E_0 from an electron gun of an electrostatic electron spectrometer in a conventional beam-beam configuration. Scattered electrons were detected by the spectrometer's electrostatic analyzer as a function of energy-loss (ΔE) and θ. The spectrometer delivered typical currents of $\approx$200–300 nA and with an energy resolution of about 170–200 meV (FWHM) in the low-resolution mode and 75–120 meV in the high-resolution mode with typical currents of $\approx$50–100 nA. This spectrometer has been proven to be stable over long periods of time (many months). The unit was baked at $\approx$110–120 °C to maintain stability against oil contamination. It was enclosed in a double μ-metal shield, which reduced the Earth's magnetic field to below 5 mG. Its data acquisition/control system was computerized (angle settings, multichannel sweep, pressure monitoring, etc.), thus allowing for the continuous (overnight) collection of data. Contact potential measurements using the He $1s2s^2$ resonance at 19.366 eV [23] enabled us to determine our incident energy to within ± 0.1 eV.

Our H gas beam source is detailed in Paolini and Khakoo [24]. The H source is an extended cavity microwave discharge of 99.999% purity H_2, operating at 2450 MHz, and used a Teflon tube to conduct the atoms to the collision region, where it was terminated by a outside-silvered glass needle (0.5 to 0.7 mm internal diameter). This source delivered H with a dissociation fraction of approximately 82–85 %. This fraction is stable over periods exceeding a month.

The method of mixtures was used here to obtain relative Ne excitation cross sections, using H as a standard, in a way similar to that described in Khakoo *et al.* [22] (The absolute normalization of these relative Ne DCS's is described later.) A 1:1 mixture (by pressure) of H_2 to Ne was typically used, and was introduced into the discharge tube through separate precision leak valves. At the working pressure (typically 0.3

Torr of H_2 and 0.3 Torr of Ne), the experimental chamber pressure increased from a base pressure of 8×10^{-8} Torr to 2×10^{-6} Torr. The gas discharge of Ne and H+H_2 was allowed to settle over a day's period. Electron energy-loss spectra simultaneously covering the ΔE regions of 9.7–10.7 eV and 16–17.5 eV (see Fig. 1), were taken at intervals of 5°. The impact energies E_0 and range of scattering angles from θ_1 to θ_2, were at $\{E_0,\theta_1,\theta_2\}$ of {20 eV, 20°, 120°}, {25 eV, 20°, 125°}, {30 eV, 20°, 125°}, {40 eV, 20°, 125°}, {50 eV, 15°, 120°} and {100 eV, 5°, 125°}. In the event that the experiment was interrupted, usually to replace the discharge tube, spectra were taken at several overlapping θ at the pertinent E_0 to establish the relative calibration between these separate data sets.

The method of mixtures using H and Ne relies on the fact that the angular profiles of the constituent gases in the gas beam are similar. In such a case, the ratio $R_{\mathrm{H/Ne}}$ of intensities of the features under the corresponding H and Ne spectra, $I^s{}_{\mathrm{H}}(E_0,\theta)$, $I^s{}_{\mathrm{Ne}}(E_0,\theta)$, respectively, at the given E_0 and θ are related to their electron impact DCS's σ as [22]

$$R_{\mathrm{H/Ne}}(E_0,\theta)=\frac{I^s_{\mathrm{H}}(E_0,\theta)}{I^s_{\mathrm{Ne}}(E_0,\theta)}=\frac{T_{\mathrm{H}}(E_R)I_0n_{\mathrm{H}}(l\Delta\Omega)_{\mathrm{eff}}\sigma_{\mathrm{H}}(E_0,\theta)}{T_{\mathrm{Ne}}(E_R)I_0n_{\mathrm{Ne}}(l\Delta\Omega)_{\mathrm{eff}}\sigma_{\mathrm{Ne}}(E_0,\theta)},\qquad(5)$$

where the subscripts H, Ne represent the constituent gases, and T is the efficiency of the scattered electron detector which is strongly dependent on the residual kinetic energy of the electrons E_R $(=E_0-\Delta E)$. I_0 is the incident electron current, n is the number density of the target gas, and $(l\Delta\Omega)_{\mathrm{eff}}$ is the overlap between the electron path length, l, and the detector solid angle, $\Delta\Omega$. This term is dependent on the profile of the gas beam at the collision region. The validity of this method is discussed further in the Appendix.

2. Relative measurements

With the profiles of the gases (H and Ne) in Eq. (5) (i.e., the $l\Delta\Omega$ terms) essentially the same, under otherwise identical experimental conditions (steady electron beam and gas beam) we have

$$R_{\mathrm{H/Ne}}(E_0,\theta)=\frac{I^s_{\mathrm{H}}(E_0,\theta)}{I^s_{\mathrm{Ne}}(E_0,\theta)}=\frac{T_{\mathrm{H}}(E_R)(dN/dt)_{\mathrm{H}}\sqrt{M_{\mathrm{H}}}\sigma_{\mathrm{H}}(E_0,\theta)}{T_{\mathrm{Ne}}(E_R)(dN/dt)_{\mathrm{Ne}}\sqrt{M_{\mathrm{Ne}}}\sigma_{\mathrm{Ne}}(E_0,\theta)},\qquad(6)$$

where dN/dt is the flow rate (s^{-1}) of the gas and M its molecular weight. Under steady state conditions (constant dN/dt, constant I_0), we measured $R_{\mathrm{H/Ne}}(E_0,\theta)$ at the E_0 and θ values discussed above. Under these conditions, the electron detector settings were left undisturbed. These values of $R_{\mathrm{H/Ne}}(E_0,\theta)$ were normalized to the $H(n=2)$ DCS's measured in Ref. [22] at $E_0\geqslant30$ eV and the theoretical $H(n=2)$ DCS's of Bray and Stelbovics [25] at $E_0\leqslant30$ eV, to obtain relative DCS's for electron impact excitation of the Ne $2p^53s$ configuration levels.

3. Absolute calibrations

The relative Ne DCS measurements were placed on an absolute scale based on the He$(2^1S+2^3P+2^1P)$ excitation DCS's at E_0 values of 30 eV and above. Below these E_0 values (where the inelastic He standard could not be used) the Ne DCS's were normalized to the Ne elastic DCS of Register and Trajmar [26]. The procedure for normalization is as follows.

(*i*) $E\geqslant30$ eV. For $E\geqslant30$ eV for He, Ne and He+Ne mixture the flow rates were measured by letting the gas or mixture fill a stagnant volume V_0 and measuring the rise in pressure, P, using a manometer connected to our laboratory computer. In this case for the individual gases

$$dN/dt=(kT/V_0)dP/dt\qquad(7)$$

and for the mixture of He and Ne

$$dN/dt_{\mathrm{He}}+dN/dt_{\mathrm{Ne}}=(kT/V_0)dP/dt,\qquad(8)$$

as is discussed in Khakoo *et al.* [27]. Thus all individual-gas flow rates and the mixed-gas flow rates were measured in sequence with one gas first, followed by the mixture of both gases, followed by the other gas last (i.e., first gas now removed). We also observed that the time taken for the flow rate to settle was long (>5 h), but its short-term systematic change could be fitted by a semiempirical formula given by

$$dP/dt(t)=a_0\exp(-a_1t)+a_2t+a_3.\qquad(9)$$

A sample of the behavior of the flow rate is given in Fig. 2. Repeated measurements of the flow rates with fitting using Eq. (9) enabled us to determine the flow rates accurately at any value of *t*. Concurrent with this, we measured electron energy-loss spectra in the range of $\Delta E=16.0$ to 22.5 eV covering both the He and Ne features of interest. Following this a spectrum with the He removed (i.e., Ne only) was taken. These spectra were taken at $\theta=40°$ to 60° and 90°. The Ne-only spectrum was used to subtract a small feature in the mixture at $\Delta E=20.6$ eV, close to the ionization potential. Figure 3 illustrates this procedure which enabled us to determine the intensity of the He$(2^1S+2^3P+2^1P)$ to better than 2% uncertainty. (This small, yet significant, overlap of the He and Ne energy-loss spectra deterred us from using He as our calibration standard at all θ, since this method incurs an additional subtraction procedure, which requires careful analysis.) Additionally, the relative normalization with H could be made at lower E_0 values since the ΔE of H ($n=2$, 10.2 eV) is less than that of He ($n=2$, 21 eV). The absolute normalization using He was therefore made at considerably fewer θ where a careful subtraction of the overlap was carried out between Ne and He. Following this, He alone was reintroduced and (without adjusting the electron detector) a spectrum of He covering the elastic scattering peak and the inelastic features with $\Delta E=19.5$ eV to 30 eV were taken at $E_0=30$ eV and $\theta=90°$. These He spectra were taken with the gas flowing through the needle and also with the gas

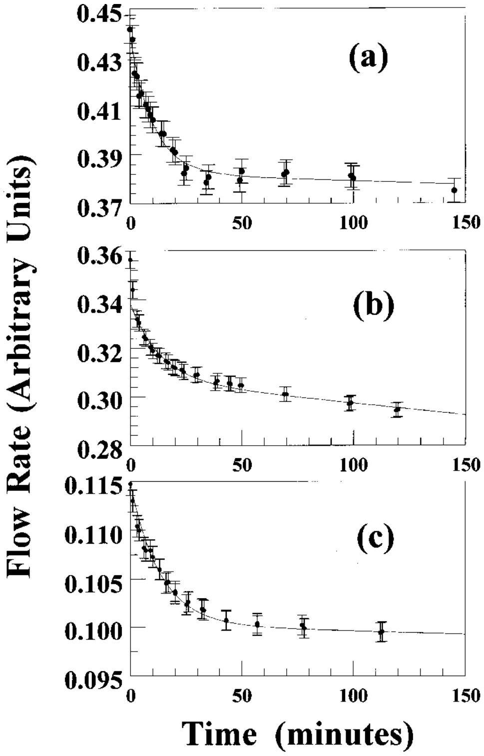

FIG. 2. Relative flow rates (dP/dt) for mixtures of Ne and He used in determining the absolute DCS's of Ne by normalization to the He DCS's of Refs. [30] and [31]. (a) Mixture of Ne/He, (b) Ne alone, and (c) He alone. The line is a least-squares fit to the data using Eq. (12). Two closely-spaced measurements are taken for each point to verify consistency.

diverted through a side leak to determine scattering backgrounds for elastic and inelastic scattering (around 8–10 %) at $\theta = 90°$. Backgrounds in the inelastic scattering channel (taken at the range of angles of this data) ranged from about 8–13 % at small $\theta \approx 10° - 20°$, but rapidly declined to 2% at $\theta > 20°$. These spectra were used to determine the detector transmission $T(E_R)$ following the discussion (based on the Wannier law) in Nickel *et al.* [28]. The values of $T(E_R)$, dN/dt, the scattering intensities of He($2^1S + 2^3P + 2^1P$) and Ne($n=3$) transitions were substituted into Eq. (6) (using He instead of H). Using the absolute He He($2^1S + 2^3P + 2^1P$) DCS's of Hall *et al.* [29] at $E = 30$, 40, and 50 eV and Trajmar *et al.* [30] and Cartwright *et al.* [30] (summed DCS's) at $E = 100$ eV, the absolute Ne($n=3$) DCS's were obtained from Eq. (6).

(*ii*) $E_0 \leqslant 30$ eV. For $E = 20$ eV and 25 eV, DCS's for the He ($n=2$) inelastic features were not available. Thus we employed the conventional calibration method based on Ne elastic scattering DCS's. Here, Ne alone was made to flow through the gas needle and also shunted through a side-leak to determine the background scattering. Energy-loss spectra covering the elastic and $n=3$ Ne features were acquired. The spectrometer detector transmission was determined [using additional He alone spectra taken at $E_0 = 30$ eV, as before in Sec. II A 3 (i) following the procedure detailed in Nickel *et al.* [28]]. The transmission-corrected ratio of the intensity of the elastic to inelastic energy-loss features was normalized to the elastic scattering DCS's of Register and Trajmar [26] at $\theta = 50°$, where these DCS's are stationary with θ and are in excellent agreement with those of Williams and Crowe [31] and Andric [(unpublished), see Ref. [26]]. At $E_0 = 25$ eV, the Register and Trajmar DCS's were interpolated between $E_0 = 20$ eV [$4.87(\pm 0.34) \times 10^{-17}$ cm^2/sr] and $E_0 = 30$ eV [$4.39(\pm 0.35) \times 10^{-17}$ cm^2/sr]. This procedure was also repeated at 30 eV to cross-check the mixed-gases' relative-flow normalization procedure followed in Sec. II A 3 (i), and agreement between the two normalization procedures was better than 11% (i.e., within the overall error bars of $\approx 13\%$). The summed absolute DCS's and their associated uncertainties are given in Tables II(a)–II(f). Table III summarizes the uncertainties invoked in measurements in Secs. II A 3 (i) and (ii).

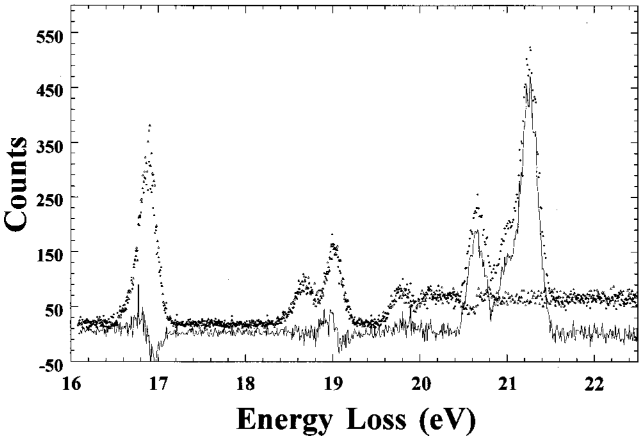

FIG. 3. Electron energy-loss spectra of (●) He and Ne taken as a mixture, (△) with Ne alone and (—) with 0.95 of (△) subtracted from (●) to eliminate the contribution of the Ne($n=3$) feature from the mixture. The spectra are taken under identical spectrometer conditions (same incident current, analyzer settings, etc.). $E_0 = 100$ eV and $\theta = 40°$. Note the residual in (—) due to the different instrumental energy resolutions in (●) and (△) as a consequence of the different target profiles for the mixture of He and Ne as compared to Ne alone. See text for details.

B. High energy-resolution experiment

In the second type of experiment, the apparatus consisted of an electron energy-loss spectrometer with double hemispherical energy selectors in both the gun and the analyzer sections as has been detailed in Guo *et al.* [3]. The spectrometer was housed in a vacuum chamber, which was pumped with a 12 in. diffusion pump. The base pressure of the vacuum chamber was 1×10^{-7} Torr. Both the gun and the analyzer sections were baked to about 120 °C during the experiment to maintain the stable conditions necessary for taking electron energy-loss spectra over long periods. To reduce the earth's magnetic field the vacuum chamber was shielded with a doubly layered high-permeability, low-field μ-metal shield and a high-field, low-permeability double μ-metal shield. The double layer shield was further demagnetized using a 0–100 A ac-driven coil (coupled to a variable transformer) in between the μ-metal layers and thus the magnetic field in the chamber could be reduced to 1–2 mG. An impor-

TABLE II. Normalized experimental DCS's and DCS ratios at different E_0 values. The second column under each heading corresponds to ±1 standard deviation estimated uncertainties. (a) $E_0=20$ eV; (b) $E_0=25$ eV; (c) $E_0=30$ eV; (d) $E_0=40$ eV; (e) $E_0=50$ eV; (f) $E_0=100$ eV. Data in italics correspond to extrapolated values using theoretical results as a guide.

(a)

Angle (deg)	DCS's (10^{-19} cm^2/sr)										DCS ratios					
	$2p^53s$		$2p^53s[3/2]_2^\circ$		$2p^53s[3/2]_1^\circ$		$2p^53s[1/2]_0^\circ$		$2p^53s[1/2]_1^\circ$		r		r'		r''	
1	*78.6*	*13.6*	*1.580*	*0.598*	*6.91*	*0.59*			*70.1*	*0.8*			0.099	0.007	0.229	0.090
2	*59.2*	*9.86*			*5.36*	*1.27*			*53.8*	*1.6*			0.100	0.024		
3	*42.5*	*6.80*	*1.58*	*0.92*	*3.99*	*0.41*	*0.32*	*0.61*	*36.6*	*1.0*	4.94	21.52	0.109	0.011	0.395	0.219
5	*25.5*	*2.88*	*1.27*	*0.64*	*2.65*	*0.57*	*0.34*	*0.40*	*21.3*	*2.8*	3.77	10.23	0.125	0.021	0.477	0.314
10	12.1	1.42	1.05	0.12	1.26	0.14	0.28	0.05	9.52	0.8	3.72	0.46	0.133	0.004	0.833	0.042
15	10.1	1.18	1.34	0.17	1.08	0.15	0.22	0.08	7.44	0.84	6.03	1.63	0.145	0.011	1.237	0.125
20	8.62	1.16	1.00	0.07	1.17	0.08	0.18	0.02	6.27	0.41	5.60	0.65	0.186	0.004	0.859	0.027
25	8.73	1.07	1.30	0.16	1.21	0.15	0.15	0.05	6.08	0.69	8.49	2.87	0.199	0.011	1.074	0.077
30	9.15	1.18	1.24	0.11	1.33	0.11	0.22	0.03	6.36	0.51	5.60	0.78	0.209	0.006	0.933	0.040
35	9.13	1.11	1.46	0.18	1.34	0.17	0.23	0.06	6.10	0.70	6.46	1.63	0.219	0.012	1.093	0.079
40	10.4	1.40	1.81	0.17	1.65	0.15	0.35	0.06	6.63	0.54	5.15	0.72	0.249	0.010	1.097	0.057
45	8.95	1.13	1.84	0.22	1.44	0.18	0.33	0.05	5.34	0.62	5.61	0.56	0.270	0.009	1.273	0.055
50	8.60	1.08	1.82	0.16	1.50	0.13	0.38	0.04	4.90	0.41	4.82	0.27	0.307	0.007	1.214	0.036
55	7.53	0.98	1.97	0.24	1.29	0.16	0.36	0.05	3.92	0.46	5.49	0.47	0.328	0.012	1.532	0.067
60	6.59	0.82	1.75	0.15	1.27	0.11	0.35	0.04	3.22	0.27	5.00	0.30	0.394	0.009	1.379	0.037
65	6.60	0.94	1.80	0.22	1.32	0.16	0.38	0.06	3.09	0.37	4.74	0.52	0.425	0.015	1.371	0.056
70	5.08	0.62	1.72	0.15	1.14	0.10	0.31	0.03	1.91	0.16	5.50	0.35	0.594	0.014	1.509	0.037
75	3.92	0.51	1.39	0.17	0.85	0.11	0.32	0.05	1.36	0.18	4.32	0.41	0.625	0.024	1.631	0.073
80	3.90	0.48	1.60	0.14	0.90	0.08	0.34	0.04	1.05	0.09	4.66	0.27	0.857	0.011	1.770	0.042
85	2.73	0.33	1.02	0.13	0.78	0.10	0.24	0.04	0.68	0.08	4.23	0.41	1.138	0.042	1.313	0.064
90	2.28	0.31	1.09	0.08	0.59	0.05	0.18	0.02	0.42	0.04	6.13	0.32	1.419	0.017	1.855	0.045
95	1.93	0.24	0.89	0.11	0.50	0.08	0.23	0.03	0.31	0.04	3.96	0.16	1.595	0.147	1.786	0.082
100	1.97	0.25	0.85	0.06	0.56	0.04	0.19	0.02	0.38	0.02	4.58	0.50	1.486	0.042	1.528	0.062
105	1.78	0.21	0.70	0.09	0.45	0.06	0.17	0.03	0.45	0.06	4.08	0.43	0.998	0.027	1.560	0.072
110	1.86	0.22	0.72	0.07	0.46	0.05	0.16	0.02	0.53	0.05	4.59	0.40	0.878	0.015	1.552	0.054
115	1.91	0.25	0.62	0.10	0.50	0.09	0.13	0.03	0.66	0.11	4.70	0.74	0.764	0.035	1.236	0.069
120	1.98	0.28	0.60	0.09	0.41	0.07	0.12	0.02	0.85	0.13	4.99	0.57	0.483	0.024	1.445	0.074
125	*2.06*	*0.29*	*0.54*	*0.09*	*0.43*	*0.07*	*0.097*	*0.024*	*0.99*	*0.15*	5.56	1.05	0.429	0.019	1.268	0.078
130	*2.40*	*0.34*	*0.61*	*0.7*	*0.45*	*0.05*	*0.077*	*0.016*	*1.26*	*0.13*	7.99	1.51	0.357	0.015	1.360	0.070

(b)

Angle (deg)	DCS's (10^{-19} cm^2/sr)										DCS ratios					
	$2p^53s$		$2p^53s[3/2]_2^\circ$		$2p^53s[3/2]_1^\circ$		$2p^53s[1/2]_0^\circ$		$2p^53s[1/2]_1^\circ$		r		r'		r''	
1	*92.0*	*15.6*	*2.79*	*0.49*	*8.47*	*1.44*	*0.41*	*0.12*	*80.3*	*13.7*	6.77	1.73	0.105	0.001	0.329	0.015
3	*78.0*	*13.26*	*2.38*	*0.33*	*7.46*	*0.99*	*0.51*	*0.11*	*67.7*	*8.8*	4.71	0.87	0.110	0.002	0.319	0.015
5	*60.0*	*10.20*	*1.80*	*0.33*	*5.59*	*1.15*	*0.65*	*0.17*	*52.0*	*8.8*	2.79	0.60	0.108	0.003	0.323	0.016
10	39.0	5.68	1.43	0.22	3.66	0.54	0.34	0.07	33.5	4.9	4.22	0.66	0.109	0.003	0.392	0.019
15	26.9	3.78	1.20	0.18	2.65	0.38	0.24	0.05	22.81	3.2	4.94	0.75	0.116	0.003	0.453	0.020
20	22.1	2.89	1.29	0.18	2.22	0.29	0.24	0.05	18.32	2.40	5.34	0.75	0.121	0.000	0.580	0.020
25	19.39	2.48	1.56	0.21	1.99	0.27	0.35	0.06	15.49	1.98	4.52	0.61	0.129	0.005	0.783	0.023
30	13.10	1.85	1.25	0.19	1.54	0.23	0.31	0.06	10.01	1.41	4.08	0.38	0.153	0.004	0.814	0.025
35	10.22	1.34	1.26	0.18	1.39	0.20	0.27	0.06	7.29	0.96	4.66	0.61	0.191	0.005	0.906	0.040
40	8.12	1.07	1.35	0.19	1.22	0.17	0.24	0.05	5.31	0.70	5.61	0.66	0.229	0.008	1.112	0.048
45	6.7	0.96	1.37	0.20	1.08	0.16	0.30	0.05	3.95	0.57	4.61	0.27	0.273	0.007	1.269	0.054
50	5.15	0.76	1.26	0.19	0.92	0.14	0.23	0.04	2.73	0.40	5.38	0.38	0.336	0.007	1.378	0.075
55	4.23	0.60	1.16	0.17	0.82	0.12	0.25	0.04	2.00	0.29	4.68	0.21	0.408	0.008	1.424	0.071
60	3.60	0.50	1.07	0.15	0.83	0.12	0.23	0.04	1.46	0.20	4.60	0.25	0.573	0.014	1.290	0.053
65	3.10	0.42	0.99	0.14	0.69	0.10	0.24	0.04	1.17	0.16	4.11	0.32	0.586	0.025	1.446	0.069
70	2.54	0.34	0.89	0.12	0.60	0.09	0.17	0.03	0.89	0.12	5.37	0.45	0.677	0.024	1.484	0.077
75	2.31	0.30	0.84	0.11	0.59	0.08	0.18	0.03	0.70	0.09	4.79	0.50	0.838	0.016	1.436	0.064
80	1.97	0.25	0.69	0.09	0.47	0.07	0.15	0.03	0.66	0.08	4.47	0.69	0.716	0.052	1.455	0.065
85	1.70	0.23	0.58	0.08	0.39	0.06	0.13	0.022	0.59	0.08	4.43	0.47	0.657	0.035	1.486	0.042
90	1.43	0.19	0.50	0.07	0.30	0.05	0.076	0.023	0.56	0.08	6.56	1.80	0.537	0.055	1.660	0.048

TABLE II. (*Continued.*)

(b)

Angle (deg)	DCS's (10^{-19} cm^2/sr)										DCS ratios					
	$2p^53s$		$2p^53s[3/2]_2^\circ$		$2p^53s[3/2]_1^\circ$		$2p^53s[1/2]_0^\circ$		$2p^53s[1/2]_1^\circ$		r		r'		r''	
95	1.31	0.17	0.35	0.05	0.26	0.04	0.078	0.017	0.62	0.08	4.50	0.51	0.415	0.019	1.358	0.049
100	1.24	0.16	0.30	0.05	0.25	0.04	0.026	0.012	0.67	0.09	11.39	5.31	0.365	0.035	1.213	0.039
105	1.20	0.17	0.24	0.04	0.15	0.03	0.053	0.014	0.76	0.11	4.51	0.72	0.199	0.015	1.577	0.059
110	1.24	0.16	0.18	0.03	0.19	0.03	0.034	0.013	0.83	0.11	5.31	1.93	0.232	0.024	0.941	0.035
115	1.25	0.16	0.17	0.03	0.17	0.03	0.073	0.016	0.85	0.11	2.29	0.49	0.196	0.021	1.008	0.030
120	1.29	0.17	0.15	0.03	0.16	0.03	0.020	0.014	0.96	0.13	7.41	3.19	0.168	0.014	0.894	0.024
125	*1.35*	*0.23*	*0.14*	*0.03*	*0.18*	*0.04*	*0.031*	*0.014*	*1.01*	*0.17*	4.50	1.98	0.175	0.020	0.784	0.022
130	*1.45*	*0.25*	*0.16*	*0.03*	*0.16*	*0.03*	*0.057*	*0.016*	*1.07*	*0.18*	2.75	0.71	0.153	0.017	0.950	0.032

(c)

Angle (deg)	DCS's (10^{-19} cm^2/sr)										DCS ratios					
	$2p^53s$		$2p^53s[3/2]_2^\circ$		$2p^53s[3/2]_1^\circ$		$2p^53s[1/2]_0^\circ$		$2p^53s[1/2]_1^\circ$		r		r'		r''	
1	*180.8*	*30.7*	*2.245*	*0.394*	*14.49*	*2.47*	*0.635*	*0.131*	*163.5*	*27.8*	3.537	0.445	0.089	0.001	0.155	0.007
3	*174.4*	*29.65*	*2.281*	*0.401*	*13.88*	*2.37*	*0.513*	*0.115*	*137.8*	*26.8*	4.448	0.677	0.088	0.001	0.164	0.008
5	*167.3*	*28.44*	*2.16*	*0.38*	*13.55*	*2.31*	*0.54*	*0.11*	*151.1*	*25.7*	4.02	0.44	0.1	0.0	0.159	0.006
8	153.1	26.02	2.21	0.39	12.78	2.18	0.56	0.12	137.5	23.4	3.96	0.57	0.09	0.0	0.173	0.008
10	142.1	18.56	2.24	0.31	11.20	1.47	0.72	0.12	127.95	16.7	3.10	0.35	0.09	0.00	0.200	0.009
15	105.7	13.81	2.52	0.34	9.08	1.20	0.68	0.11	93.46	12.21	3.69	0.38	0.10	0.00	0.278	0.012
20	58.04	7.58	1.85	0.26	5.30	0.71	0.51	0.09	50.39	6.58	3.66	0.50	0.11	0.00	0.349	0.020
25	35.62	4.65	1.98	0.27	3.57	0.48	0.39	0.07	29.68	3.88	5.05	0.71	0.12	0.00	0.555	0.030
30	19.00	2.48	1.73	0.24	2.10	0.29	0.31	0.06	14.86	1.94	5.61	0.82	0.14	0.01	0.825	0.050
35	13.16	1.72	1.56	0.22	1.67	0.23	0.28	0.05	9.65	1.26	5.59	0.83	0.17	0.01	0.937	0.060
40	7.4	0.97	1.16	0.17	1.09	0.16	0.32	0.06	4.86	0.64	3.57	0.47	0.22	0.01	1.067	0.083
45	6.35	0.91	1.31	0.20	1.07	0.17	0.33	0.06	3.64	0.52	3.96	0.50	0.29	0.02	1.228	0.093
50	4.71	0.61	1.16	0.16	0.83	0.12	0.23	0.04	2.48	0.32	5.12	0.55	0.33	0.02	1.402	0.078
55	4.52	0.59	1.30	0.17	0.92	0.12	0.24	0.04	2.07	0.27	5.52	0.42	0.44	0.01	1.422	0.053
60	3.68	0.48	1.15	0.16	0.76	0.11	0.23	0.04	1.54	0.20	5.01	0.56	0.50	0.03	1.504	0.097
65	3.13	0.41	0.99	0.13	0.72	0.10	0.19	0.04	1.23	0.16	5.11	0.65	0.59	0.03	1.377	0.080
70	2.88	0.38	0.99	0.13	0.62	0.09	0.15	0.03	1.12	0.15	6.65	1.04	0.55	0.04	1.605	0.108
75	2.43	0.32	0.70	0.09	0.53	0.08	0.15	0.03	1.05	0.14	4.56	0.77	0.50	0.04	1.337	0.110
80	2.00	0.26	0.60	0.09	0.40	0.05	0.12	0.03	0.88	0.11	4.98	0.97	0.45	0.01	1.506	0.107
85	1.66	0.22	0.46	0.06	0.30	0.04	0.064	0.013	0.84	0.11	7.18	1.15	0.35	0.02	1.546	0.112
90	1.33	0.17	0.24	0.04	0.22	0.04	0.050	0.019	0.82	0.11	4.82	1.65	0.27	0.03	1.116	0.181
95	1.23	0.16	0.14	0.03	0.19	0.04	0.058	0.021	0.85	0.11	2.35	0.81	0.22	0.03	0.734	0.160
100	1.15	0.15	0.12	0.02	0.12	0.02	0.021	0.008	0.90	0.12	5.52	2.00	0.14	0.01	0.946	0.135
105	1.12	0.15	0.07	0.02	0.13	0.02	0.022	0.010	0.90	0.12	3.29	3.58	0.14	0.01	0.565	0.104
110	1.19	0.15	0.06	0.01	0.13	0.02	0.015	0.010	0.98	0.13	2.71	2.55	0.13	0.01	0.444	0.112
115	1.37	0.18	0.10	0.02	0.14	0.02	0.014	0.006	1.12	0.15	6.75	2.95	0.13	0.01	0.673	0.085
120	*1.44*	*0.19*	*0.12*	*0.02*	*0.14*	*0.03*	*0.047*	*0.015*	*1.13*	*0.15*	*2.56*	*1.02*	*0.13*	*0.01*	*0.840*	*0.144*
125	*1.82*	*0.30*	*0.13*	*0.03*	*0.22*	*0.04*	*0.040*	*0.011*	*1.44*	*0.24*	*3.15*	*1.04*	0.15	0.01	0.580	0.090
130	2.14	0.36	0.145	0.030	0.250	0.047	0.042	0.015	1.699	0.289	3.485	1.483	0.147	0.015	0.579	0.104

(d)

Angle (deg)	DCS's (10^{-19} cm^2/sr)										DCS ratios					
	$2p^53s$		$2p^53s[3/2]_2^\circ$		$2p^53s[3/2]_1^\circ$		$2p^53s[1/2]_0^\circ$		$2p^53s[1/2]_1^\circ$		r		r'		r''	
1	*341*	*57.8*	0.802	0.240	25.6	4.4	0.162	0.035	314	53	4.950	*1.112*	0.081	*0.001*	0.031	*0.002*
3	*315*	*53.6*	0.828	0.175	24.0	4.1	0.264	0.129	290	49	3.134	*0.694*	0.083	*0.001*	0.034	*0.003*
5	*280*	*47.6*	0.898	0.165	20.6	3.5	0.170	0.064	258	44	5.268	*1.502*	0.080	*0.001*	0.044	*0.002*
8	*240*	*40.8*	1.009	0.180	18.2	3.1	0.252	0.060	221	37	4.010	*0.779*	0.082	*0.001*	0.056	*0.004*
10	184	22.8	0.955	0.123	14.1	1.7	0.220	0.035	169	21	4.339	*0.461*	0.083	*0.001*	0.068	*0.002*
15	121	16.5	1.186	0.161	7.92	1.06	0.220	0.035	112	15	5.383	*0.425*	0.071	*0.001*	0.150	*0.004*
20	50.0	6.5	0.844	0.112	4.00	0.52	0.201	0.034	45.0	5.9	4.206	*0.465*	0.089	*0.000*	0.211	*0.006*
25	27.1	3.5	1.110	0.150	2.40	0.32	0.283	0.048	23.3	3.04	3.928	*0.482*	0.103	*0.003*	0.463	*0.021*

TABLE II. (*Continued.*)

(d)

Angle (deg)	DCS's (10^{-19} cm^2/sr)										DCS ratios					
	$2p^53s$		$2p^53s[3/2]_2^\circ$		$2p^53s[3/2]_1^\circ$		$2p^53s[1/2]_0^\circ$		$2p^53s[1/2]_1^\circ$		r		r'		r''	
30	14.2	1.90	1.010	0.137	1.48	0.20	0.223	0.034	11.5	1.5	4.524	*0.398*	0.130	*0.001*	0.680	*0.019*
35	8.93	1.17	1.215	0.165	1.19	0.16	0.244	0.042	6.28	0.83	4.978	*0.648*	0.189	*0.008*	1.023	*0.060*
40	5.77	0.71	0.989	0.125	0.844	0.108	0.190	0.030	3.75	0.46	5.207	*0.544*	0.225	*0.008*	1.172	*0.056*
45	5.07	0.69	1.050	0.149	0.864	0.126	0.200	0.038	2.95	0.40	5.254	*0.763*	0.292	*0.016*	1.215	*0.085*
50	3.99	0.50	0.899	0.116	0.716	0.093	0.183	0.027	2.19	0.28	4.928	*0.373*	0.326	*0.010*	1.257	*0.049*
55	3.56	0.48	0.852	0.116	0.643	0.088	0.180	0.26	1.89	0.25	4.746	*0.285*	0.341	*0.007*	1.326	*0.033*
60	3.06	0.40	0.728	0.095	0.574	0.075	0.157	0.023	1.60	0.21	4.644	*0.320*	0.360	*0.007*	1.267	*0.035*
65	2.54	0.32	0.609	0.080	0.449	0.060	0.127	0.020	1.36	0.17	4.796	*0.392*	0.331	*0.013*	1.356	*0.058*
70	2.17	0.30	0.481	0.069	0.406	0.059	0.119	0.020	1.17	0.16	4.042	*0.452*	0.347	*0.014*	1.185	*0.070*
75	1.76	0.23	0.361	0.049	0.306	0.042	0.068	0.010	1.03	0.14	5.339	*0.481*	0.279	*0.010*	1.179	*0.049*
80	1.54	0.21	0.276	0.038	0.225	0.031	0.060	0.009	0.982	0.132	4.613	*0.435*	0.230	*0.009*	1.226	*0.060*
85	1.21	0.15	0.168	0.025	0.166	0.024	0.025	0.009	0.850	0.104	6.804	*0.779*	0.196	*0.015*	1.009	*0.111*
90	1.05	0.14	0.097	0.015	0.129	0.019	0.020	0.006	0.808	0.106	4.794	*1.640*	0.160	*0.012*	0.751	*0.081*
95	0.92	0.12	0.062	0.010	0.097	0.015	0.017	0.005	0.747	0.099	3.566	*1.144*	0.129	*0.010*	0.639	*0.067*
100	0.90	0.12	0.060	0.009	0.089	0.012	0.012	0.003	0.738	0.096	4.993	*1.130*	0.120	*0.006*	0.677	*0.049*
105	0.88	0.11	0.060	0.008	0.091	0.012	0.013	0.004	0.712	0.093	4.506	*1.612*	0.128	*0.005*	0.656	*0.042*
110	0.92	0.11	0.075	0.010	0.098	0.013	0.012	0.003	0.739	0.091	6.530	*1.672*	0.133	*0.007*	0.766	*0.055*
115	0.97	0.12	0.083	0.011	0.102	0.014	0.014	0.004	0.773	0.098	5.915	*1.380*	0.132	*0.006*	0.817	*0.057*
120	1.09	0.15	0.098	0.015	0.116	0.018	0.029	0.007	0.848	0.115	3.415	*0.675*	0.137	*0.009*	0.845	*0.082*
125	*1.30*	*0.22*	0.099	0.018	0.148	0.027	0.028	0.007	1.025	0.174	3.529	*0.713*	0.145	*0.009*	0.669	*0.061*
130	*1.60*	*0.27*	0.114	0.020	0.179	0.032	0.019	0.006	1.288	0.219	5.894	*1.878*	0.139	*0.008*	0.635	*0.056*

(e)

Angle (deg)	DCS's (10^{-19} cm^2/sr)										DCS ratios					
	$2p^53s$		$2p^53s[3/2]_2^\circ$		$2p^53s[3/2]_1^\circ$		$2p^53s[1/2]_0^\circ$		$2p^53s[1/2]_1^\circ$		r		r'		r''	
1	*650*	*111*	*0.312*	*0.079*	*48.545*	*8.253*	*0.102*	*0.076*	*600.921*	*102.161*	3.057	2.498	0.081	0.001	0.006	0.001
3	*600*	*102*	*0.217*	*0.047*	*44.436*	*7.554*	*0.100*	*0.086*	*555.135*	*94.373*	2.167	2.396	0.080	0.001	0.005	0.001
5	*550*	*94*	*0.245*	*0.083*	*40.275*	*7.470*	*0.108*	*0.186*	*509.002*	*94.397*	2.279	2.115	0.079	0.001	0.006	0.001
8	*400*	*68*	*0.429*	*0.122*	*29.698*	*6.942*	*0.206*	*0.122*	*369.437*	*86.356*	2.086	1.993	0.080	0.001	0.014	0.001
10	338	43	0.545	0.078	25.061	3.191	0.137	0.052	312.289	39.765	3.976	2.460	0.080	0.001	0.022	0.001
15	153	18	0.764	0.091	11.528	1.331	0.194	0.026	140.694	16.241	3.947	1.414	0.082	0.001	0.066	0.002
20	62.5	7.9	0.899	0.118	4.985	0.633	0.212	0.033	56.382	7.158	4.274	0.504	0.088	0.001	0.180	0.007
25	26.2	3.0														
30	13.0	1.5	1.040	0.121	1.408	0.163	0.244	0.030	10.321	1.187	4.257	0.219	0.136	0.002	0.738	0.018
35	7.17	0.86	0.943	0.114	0.968	0.117	0.197	0.026	5.067	0.605	4.790	0.294	0.191	0.004	0.974	0.029
40	5.38	0.69	0.843	0.111	0.843	0.112	0.164	0.026	3.532	0.451	5.146	0.499	0.239	0.008	1.000	0.047
45	4.32	0.50														
50	3.80	0.47	0.677	0.085	0.616	0.077	0.141	0.019	2.371	0.295	4.799	0.236	0.260	0.004	1.100	0.026
55	3.22	0.37														
60	2.78	0.35	0.523	0.075	0.452	0.067	0.095	0.022	1.710	0.217	5.507	1.158	0.264	0.020	1.158	0.118
65	2.38	0.28														
70	2.00	0.24	0.359	0.045	0.278	0.036	0.075	0.012	1.292	0.152	4.812	0.598	0.216	0.011	1.288	0.085
75	1.72	0.22														
80	1.45	0.17	0.205	0.027	0.188	0.025	0.036	0.008	1.019	0.121	5.626	1.041	0.184	0.011	1.091	0.091
85	1.20	0.14														
90	1.05	0.12	0.118	0.015	0.141	0.018	0.026	0.005	0.762	0.088	4.462	0.795	0.185	0.010	0.837	0.068
95	0.86	0.10														
100	0.92	0.10	0.136	0.018	0.113	0.015	0.034	0.007	0.636	0.072	4.033	0.709	0.178	0.013	1.203	0.113
105	0.77	0.09	0.114	0.017	0.105	0.016	0.029	0.007	0.522	0.064	3.981	0.961	0.202	0.018	1.085	0.131
110	0.79	0.10	0.121	0.016	0.134	0.017	0.025	0.005	0.511	0.062	4.903	0.775	0.262	0.012	0.908	0.058
115	0.80	0.10	0.130	0.018	0.103	0.015	0.034	0.006	0.537	0.070	3.854	0.580	0.192	0.012	1.260	0.103
120	0.84	0.11	0.107	0.016	0.112	0.017	0.022	0.006	0.600	0.079	4.751	1.226	0.187	0.014	0.951	0.099
125	0.90	0.15														
130	1.00	0.17	0.078	0.020	0.112	0.028	0.018	0.007	0.792	0.190	4.448	1.320	0.141	0.010	0.698	0.079

TABLE II. (*Continued.*)

(f)

	DCS's (10^{19} cm^2/sr)										DCS ratios					
Angle (deg)	$2p^5 3s$		$2p^5 3s[3/2]_2^\circ$		$2p^5 3s[3/2]_1^\circ$		$2p^5 3s[1/2]_0^\circ$		$2p^5 3s[1/2]_1^\circ$		r		r'		r''	
1	*2628.209*	*447.000*	*0.090*	*0.024*	*195.180*	*33.185*	*0.018*	*0.004*	*2431.639*	*413.379*			0.080	0.001	0.0005	0.0151
3	*2018.153*	*343.000*	*0.115*	*0.030*	*146.153*	*24.917*	*0.023*	*0.005*	*1871.464*	*318.149*			0.078	0.001		
5	*1278.293*	*218.000*	*0.160*	*0.039*	*91.839*	*15.646*	*0.032*	*0.007*	*1186.012*	*201.622*			0.077	0.001		
8	*555.775*	*90.700*	*0.234*	*0.053*	*40.171*	*6.857*	*0.047*	*0.008*	*515.127*	*87.572*			0.078	0.001		
10	284.439	46.300	0.231	0.044	20.731	3.390	0.0342	0.0206	263.304	42.930	6.754	2.369	0.079	0.001	0.011	0.001
15	59.585	9.854	0.299	0.056	4.430	0.735	0.0709	0.0224	54.706	9.059	4.220	0.849	0.081	0.001	0.068	0.004
20	16.172	2.588	0.337	0.057	1.281	0.214	0.0752	0.0108	14.405	2.316	4.478	0.703	0.089	0.002	0.263	0.014
25	4.790	0.745	0.188	0.031	0.398	0.064	0.0397	0.0067	4.117	0.646	4.739	0.847	0.097	0.004	0.472	0.031
30	2.599	0.396	0.135	0.022	0.250	0.040	0.0170	0.0043	2.154	0.334	7.928	2.137	0.116	0.004	0.540	0.033
35	2.240	0.307	0.103	0.015	0.196	0.028	0.0192	0.0017	1.890	0.263	5.380	0.686	0.103	0.003	0.529	0.029
40	1.635	0.212	0.046	0.007	0.139	0.019	0.0090	0.0032	1.402	0.186	5.164	2.158	0.099	0.005	0.333	0.037
45	1.139	0.151	0.030	0.006	0.079	0.012	0.0091	0.0027	1.021	0.135	3.339	1.096	0.077	0.005	0.383	0.056
50	0.929	0.121	0.027	0.005	0.074	0.011	0.0078	0.0020	0.794	0.107	3.431	1.657	0.093	0.005	0.359	0.058
55	0.581	0.077	0.015	0.004	0.047	0.008	0.0067	0.0027	0.513	0.068	2.305	0.996	0.091	0.009	0.330	0.079
60	0.480	0.061	0.022	0.004	0.042	0.006	0.0086	0.0017	0.383	0.051	2.590	0.661	0.110	0.007	0.533	0.063
65	0.470	0.057	0.025	0.005	0.032	0.006	0.0043	0.0026	0.371	0.049	5.796	4.128	0.085	0.012	0.783	0.175
70	0.312	0.042	0.022	0.004	0.038	0.006	0.0037	0.0016	0.249	0.033	5.886	3.582	0.153	0.011	0.574	0.075
75	0.254	0.033														
80	0.267	0.030	0.030	0.006	0.026	0.005	0.0097	0.0018	0.161	0.021	3.156	1.046	0.160	0.022	1.183	0.221
85	0.199	0.026														
90	0.202	0.022	0.043	0.006	0.024	0.003	0.0082	0.0014	0.093	0.012	5.212	1.787	0.255	0.012	1.787	0.216
95	0.174	0.022	0.047	0.007	0.038	0.006	0.0072	0.0025	0.082	0.012	6.569	34.127	0.462	0.061	1.244	0.156
96											4.559	0.654	0.462	0.027	1.453	0.091
100	0.212	0.022	0.057	0.008	0.038	0.005	0.0075	0.0020	0.068	0.009	7.595	2.770	0.552	0.037	1.508	0.093
105	0.223	0.024	0.064	0.008	0.041	0.005	0.0139	0.0014	0.069	0.009	4.575	0.796	0.584	0.030	1.572	0.088
107											6.486	1.480	0.465	0.023	1.757	0.064
110	0.207	0.026	0.058	0.008	0.034	0.005	0.0138	0.0056	0.101	0.013	4.218	0.750	0.338	0.022	1.699	0.138
115	0.240	0.030														
120	0.248	0.031	0.042	0.006	0.033	0.004	0.0075	0.0034	0.166	0.021	5.568	2.897	0.201	0.014	1.258	0.081
125	0.381	0.064	0.035	0.013	0.041	0.015	0.0060	0.0056	0.299	0.051	5.950	51.765	0.137	0.043	0.864	0.393
130	*0.478*	*0.081*	*0.026*	*0.006*	*0.035*	*0.006*	*0.0101*	*0.0041*	*0.406*	*0.069*	2.582	1.068	0.087	0.005	0.735	0.103

tant feature of this spectrometer is the absence of "wings" in the instrumental profile, often seen in spectrometers with single hemispherical analyzers (e.g., that used in Sec. II A here). This characteristic enabled us to resolve the weak metastable energy-loss features from the stronger allowed transitions in Ne. The spectrometer operated at an energy resolution of 25–40 meV (FWHM) with an electron current ranging from 3–20 nA. It could observe scattered electrons at scattering angles up to 130°. Contact potential measurements using the He $1s2s^2$ resonance enabled us to calibrate our incident energy to well within ±0.05 eV.

Similar to the low-resolution spectrometer described in Sec. II A, this apparatus was computer controlled to enable efficient data acquisition. The computer processed the multichannel scaling measurement of the energy-loss scan as well as controlled the scattering angle positioning. It monitored the pressure behind the gas line and modulated the gas beam via a thin molybdenum beam flag. Analysis of the measured spectra was done off-line. A well-tested multi-Gaussian unfolding program (Khakoo *et al.* [1,3,4]) was used to unfold the spectra. The energy-loss levels of Ne from Moore's spectroscopy tables (Moore [32]) were used in the unfolding program. A typical electron energy-loss spectrum of Ne with typical unfolding is shown in Fig. 4. Characteristic reduced chi-squared (χ_ν^2) values of the fits to the spectra were in the range of 1–3. The separated intensities of the individual features of the Ne ($n=3$) levels were used directly to calculate the ratios in Eq. (1). Several spectra were taken at each angle to check reproducibility and to improve statistics. These relative intensities were summed and normalized directly to the summed absolute DCS's determined in Sec. II A. The present experimental data (summed and individual level DCS's) are summarized in Tables II(a)–II(f). Spectra taken at those θ not covered in the low-resolution measurements (cf. Sec. II A), were normalized to extrapolated summed Ne DCS's, using results from present models UFOMBT, *R*-matrix, DWBA and RDWA and the experimental DCS's of Brunger [18] at small θ. Table III summarizes the uncertainties invoked in measurements in Sec. II B.

III. THEORETICAL MODELS

The theoretical approaches used for comparison with the experimental data are the nonperturbative *R*-matrix approach

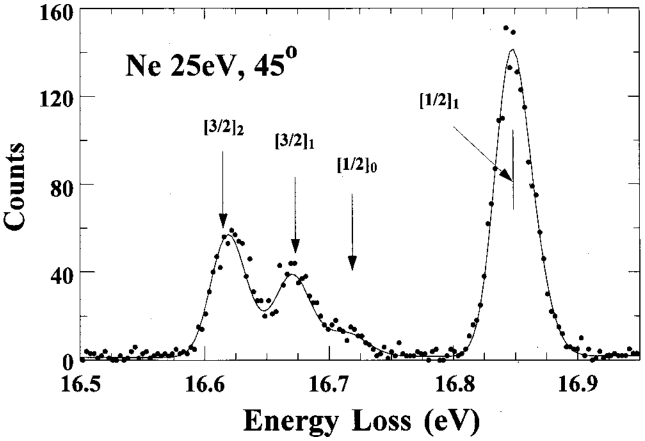

FIG. 4. High resolution spectrum of Ne at $E_0 = 25$ eV and $\theta = 45°$ showing the four levels comprising the $2p^5 3s$ configuration, and the unfolding fit using the $(2p^5 3s)[1/2]^{\circ}_1$ feature at 16.848 eV energy loss.

and the first-order distorted-wave Born approximation (DWBA). In principle, the *R*-matrix (close-coupling) approach should be valid for any energy of the projectile electron. However, numerical considerations limit the range of practical applications to lower incident energies. The DWBA, on the other hand, is expected to be valid for higher energies. It will become unreliable for incident energies approaching threshold since higher order effects are known to become increasingly important near threshold. Ideally, one could use the *R*-matrix approach for low energies, the DWBA for high energies, and the two theories would yield the same results for intermediate energies. Unfortunately, we do not live in an ideal world.

Three different DWBA approaches are investigated in this work—the semirelativistic UFOMBT, the semirelativistic DWBA, and the fully relativistic RDWA. In principle, the primary difference between the DWBA approaches lies in the treatment of relativistic effects (which one would expect should be small for scattering from neon). However, in addition to relativistic effects, there are other more subtle differences between the three approaches that can also be important. The results of a distorted-wave calculation fundamentally depend upon two input parameters—the atomic wave functions and the distorting potentials used to calculate the continuum wave functions. Two potentials enter the calculation—the potential for the incoming electron U_i and the potential for the final state electron U_f. Consequently, different distorted-wave calculations can differ in both the method used to calculate the atomic wave functions and the choice of distorting potentials.

Logically, one would expect that the potential used for the incoming electron would be the potential for the ground state of the atom and the potential used for the final state would be the potential of the excited atomic state. However, in the UFOMBT approach, the formalism requires that the ground state potential be used for both the incoming and outgoing projectile electrons. In the standard DWBA, there are, in principle, no restrictions on these potentials and practical experience suggests that one often gets better agreement with

TABLE III. Summary of experimental uncertainties in % (1 standard deviation). The 20 and 25 eV DCS's were normalized to Ne elastic scattering [26]. The 40, 50, and 100 eV DCS's were normalized to the He inelastic DCS's of Refs. [29] and [30]. The 30 eV DCS's were normalized to both Ne elastic and He inelastic standards.

Energy eV	Flow rates He/Ne	Electron current	Discharge stability	Transmission Ne to He energy loss or elastic	*H* DCS's relative	Absolute standard DCS's He/Ne	Statistical uncertainty $2p^5 3s$	Statistical uncertainty and unfolding $2p^5 3s[3/2]_2^{\circ}$	Statistical uncertainty and unfolding $2p^5 3s[3/2]_1^{\circ}$	Statistical uncertainty and unfolding $2p^5 3s[1/2]_0^{\circ}$	Statistical uncertainty and unfolding $2p^5 3s[1/2]_1^{\circ}$	Nominal overall summed $2p^5 3s$	Nominal overall error $2p^5 3s[3/2]_2^{\circ}$	Nominal overall error $2p^5 3s[3/2]_1^{\circ}$	Nominal overall error $2p^5 3s[1/2]_0^{\circ}$	Nominal overall error $2p^5 3s[1/2]_1^{\circ}$
20	2	2	3	3	5	7	9	10.5	11	18.5	4	12.5	16.3	16.6	22.3	13.1
25	2	2	3	3	5	11	5	3	3.5	20	1	13.1	13.5	13.6	23.9	13.2
30	2	2	3	3	5	7	5	8	8	21	2	10.0	12.8	12.8	23.3	10.2
40	2	2	3	3	5	13	5	6	6.5	19.5	2	14.8	16.0	16.2	24.5	15.0
50	2	2	3	3	5	13	4	5	5	15	2	14.5	15.4	15.4	20.9	14.7
100	2	2	3	3	5	12	4	10	9	28	1	13.6	16.9	16.3	31.1	13.7

experiment if the final (excited) state potential is used for both the initial and final states of the projectile electron. Consequently, this is the procedure used in the semirelativistic DWBA as well as relativistic RDWA.

Furthermore, the results of a calculation can also depend strongly on the choice for atomic wave functions. A potential advantage of the DWBA approach over the standard *R*-matrix approach is that the calculation is performed for one final atomic state at a time, i.e., wave functions can be generated which are optimized for the accuracy of the particular states of interest. This means, for example, that a $(2p^53s)\ ^1P$ state could have a different $3s$ wave function than a $(2p^53s)\ ^3P$. In a close-coupling approach, on the other hand, one simultaneously obtains cross sections for transitions between all the states used in the expansion of the wave function. While this is a very effective way of calculating data for many transitions, it also means that all four states contained in the $(2p^53s)$ manifold will have to be represented by the same $3s$ wave function. Although this $3s$ wave function might represent the best average wave function for the manifold, it may not be a particularly good wave function for any individual state. In principle, these shortfalls can be overcome by including so-called pseudo-orbitals, by extending the theory to allowing for the use of nonorthogonal orbitals, or by repeating the calculation targeting certain transitions with specially optimized target descriptions. All these solutions, however, are associated with substantial difficulties in practical applications, the most important one being limited computational resources.

A. *R*-matrix

The details of the *R*-matrix calculation for *e*-Ne scattering were presented by Zeman and Bartschat [33]. In the present paper, we show results obtained in a 31-state semirelativistic model, including all the physical states with configurations $2p^6$, $2p^53s$, $2p^53p$, $3p^53d$, and $2p^54s$, respectively, in the close-coupling expansion. Furthermore, relativistic effects were accounted for through the one-body terms of the Breit-Pauli Hamiltonian, as implemented in the Belfast version of the *R*-matrix codes (Berrington *et al.* [34]). Although not shown in the present paper, we also performed a smaller 15-state calculation, including only the lowest 15 states with configurations $2p^6$, $2p^53s$, and $2p^53p$, and even a 5-state calculation only including the states generated from $2p^6$ and $2p^53s$. It is worth noting that the singlet-triplet mixing coefficients for the two $J=1$ states, $(2p^53s)\ ^1P_1$ and $(2p^53s)\ ^3P_1$, are very similar in all these structure models, namely $\alpha=0.985$ and $\beta=0.175$. Note that the same $2p$ and $3s$ orbitals and mixing coefficients from these *R*-matrix calculations were also used in one of the semirelativistic distorted wave approaches described below. Consequently, differences between the results from those two models are predominantly reflecting the importance of channel-coupling effects.

B. Unitarized first-order many body theory

A description of a typical unitarized first-order many body theory calculation can be found in Ref. [3] and the references therein. The UFOMBT approach uses a non-relativistic collisional scheme along with a semirelativistic representation of target states. For the present calculations, an 11-configuration basis set was used: $2p^6$, $2p^53s$, $2p^53p$, $2p^53d$, $2p^54s$, $2p^54p$, $2p^55s$, $2s2p^63s$, $2s2p^63p$, $2s2p^63d$, and $2s2p^64s$. Such a large number of configurations was included in anticipation of calculating excitation of levels that originate from configurations that are energetically beyond the $2p^53s$. However, for the present case only the $2p^6$ and $2p^5\ 3s$ configurations are necessary to obtain converged results and such 2-configuration calculations do not differ appreciably from the 11-configuration values presented here.

C. Semirelativistic distorted-wave Born approximation

The semirelativistic first order distorted-wave approximation used here is based upon the work of Madison and Shelton [35] and Bartschat and Madison [36]; these results are labeled DWBA. The details of this theory may be found in the references. In this approach, a semirelativistic representation of target states is used as well as a semirelativistic representation of the continuum states for the projectile. As mentioned above, the excited state potential is used to calculate the continuum wave function for both the initial and final states of the projectile electron. We have performed calculations using two different sets of atomic wave functions. For the first case (labeled HF-DWBA), we used the Froese-Fischer [37] Hartree-Fock code to calculate the atomic wave functions. For this case we used the mixing coefficients $\alpha=0.965$ and $\beta=0.263$ from experiment [39, see Table V]. For the second calculation, we have used the same CIV3-15 state wave functions that were used in the *R*-matrix calculation mentioned above with mixing coefficients ($\alpha=0.985$, $\beta=0.175$); this calculation is labeled CIV3-15-DWBA. The purpose of the HF-DWBA calculation is to perform a DWBA calculation with wave functions optimized on each final state and the purpose of the second calculation is to see whether the DWBA and *R*-matrix approaches using the same wave functions will yield the same cross sections for intermediate energies.

D. Relativistic distorted-wave approximation

The theoretical description of the RDWA as applied to the excitation of the noble gases is given in Zuo *et al.* [16]. Since our calculations are based on the Dirac equations, we describe the target states in *j-j* coupling. We have carried out two separate calculations. The first, labeled SCGS (single-configuration ground state), involves the ground state configuration $2\overline{p}^22p^4$ and the two excited state configurations $2\overline{p}2p^43s$ and $2\overline{p}^22p^33s$ which give rise to the four fine-structure levels of the first excited P state. In the second calculation, MCGS (multiconfiguration ground state), we added the $2\overline{p}2p^43\overline{p}$ and $2\overline{p}^22p^33p$ configurations to the

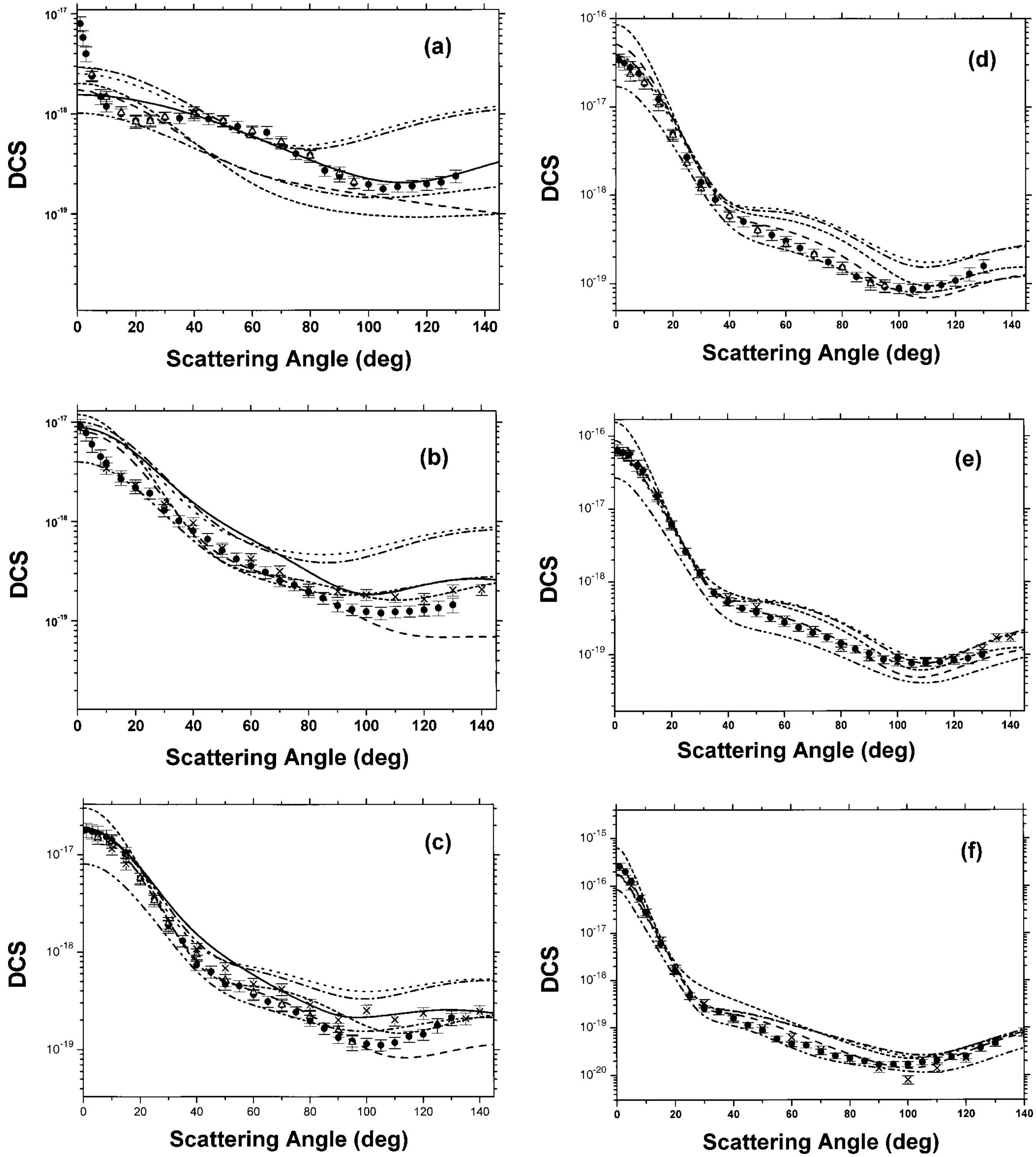

FIG. 5. DCS's for the electron impact excitation of the summed $2p^5 3s$ feature in Ne. Experiments: ●, present data with error bars; △, Brunger [18] with error bars; ×, Register *et al.* [8] with error bars. Theories: —, *R*-matrix method; – – –, UFOMBT; - - -, CIV3-15-DWBA; - - -, HF-DWBA; – - – -, SCGS-RDWA; - - -, MCGS-RDWA. (a) $E_0 = 20$ eV, (b) $E_0 = 25$ eV, (c) $E_0 = 30$ eV, (d) $E_0 = 40$ eV, (e) $E_0 = 50$ eV, and (f) $E_0 = 100$ eV. See also Tables II(a)–II(f) and text for discussion.

ground state. We also carried out calculations which included configurations involving the $3d$ and $4s$ orbitals but these did not improve our results and are not included here. In all cases we used the excited state potential as the distortion potential.

Our wave functions were calculated using the multiconfiguration Dirac-Fock program GRASP92 [38]. The same orbitals are used in the wave functions for all the target states. We can obtain the singlet-triplet mixing coefficients referred to above by transforming our wave functions to *LS* coupling. For the SCGS we obtained mixing coefficients of (0.970, 0.249) which are quite close to the values obtained from optical measurements [see Table V].

E. Mixing coefficients and tests of wave functions

Recall that the relative signs of the mixing coefficients depend on the coupling scheme. Using the notation of Eq. (2), the $(LS)_J$-coupling scheme gives the same sign for α and β whereas in the case of an $(SL)_J$-coupling yields opposite signs. In addition, in multi-configuration wave functions, it is clear that Eq. (4) does not tend to the simple optical α^2/β^2 limit, but rather to a more complicated ratio of dipole matrix elements squared. Consequently, for such multiconfiguration wave functions, Eq. (4) is not a rigorous test of these wave functions. In addition, for the multiconfigurational ground state wave function used by the RDWA, the definition of mixing coefficients (in as far as predicting the optical limit) in terms of α and β is not strictly applicable.

IV. RESULTS AND DISCUSSION

A. Summed $2p^53s$ DCS's

Figures 5(a)–5(f) show our summed DCS's for the electron impact excitation of the $2p^6 \rightarrow 2p^53s$ configuration of Ne at the E_0 and θ values discussed above. These DCS's are compared to the unpublished measurements of Brunger [18] and the earlier measurements of Register *et al.* [8]. The measurements are also compared to our UFOMBT calculations, semirelativistic *R*-matrix model, the DWBA, and the RDWA.

At $E_0 = 20$ eV [Fig. 5(a)] excellent agreement between the present DCS's and those of Brunger [18] is observed. In fact, excellent agreement for our data with the DCS's of Brunger [18] was found for all the E_0 values and θ values. These DCS's show a pronounced dip at around $\theta = 20°$, with a steeply rising DCS at $\theta < 10°$. The *R*-matrix method also shows excellent agreement with the experimental DCS's at $\theta \geqslant 40°$, but misses the dip at $\theta < 40°$. The *R*-matrix is expected to do the best here because this E_0 is below that of the ionization energy, and only a finite number of channels are open to the projectile electron. The UFOMBT, DWBA, and RDWA models all do not do well, as expected, since this E_0 is too low for reliable application of such perturbative-type, intermediate energy theories.

At $E_0 = 25$ eV [Fig. 5(b)] excellent agreement between the present DCS's and those of Register *et al.* [8] is found for $\theta < 90°$. However, at $\theta \geqslant 90°$, their DCS's exceed the present by almost 50%. Agreement with all models is unsatisfactory. The *R*-matrix gives a good shape but exceeds the experimental DCS's by at least 50%. Clearly seen in the experimental data is the point of inflexion in the DCS's at $\theta = 20°$ which evolves into the pronounced structure at this θ at $E_0 = 20$ eV [cf. Fig. 5(a)]. There is improved agreement with the UFOMBT calculations as compared to $E_0 = 20$ eV [cf. Fig. 5(a)], but the level remains qualitative at best. Both DWBA models are significantly higher in magnitude than the experimental data. The SCGS-RDWA does marginally better than the MCGS-RDWA.

At $E_0 = 30$ eV [Fig. 5(c)], the Register *et al.* [8] DCS's show good agreement with the present DCS's at forward θ, but deviate from the present DCS's at $\theta \geqslant 70°$. At this point, the *R*-matrix (which deviates from the present results and Register *et al.* for $\theta \leqslant 70°$) shows excellent agreement with the Register *et al.* DCS's for larger θ. However, we question this agreement as our present DCS's at this E_0 have been doubly normalized using both the Ne elastic-to-inelastic normalization and the method of mixtures of Ne with He. Additionally, the excellent agreement between the present DCS's and those of Brunger [18] [Fig. 5(c)] supports the reliability of the present data. The UFOMBT also shows reasonable agreement with the present DCS's with excellent quantitative agreement for $\theta \leqslant 70°$, but dropping away from our DCS at larger θ. The DWBA remains significantly higher in magnitude than the experimental DCS's while the MCGS-RDWA does better than the SCGS-RDWA, showing good qualitative agreement with experiment.

At $E_0 = 40$ eV [Fig. 5(d)], the UFOMBT, DWBA, and RDWA results show significant improvement with our corresponding DCS's over that from $E_0 = 30$ eV with excellent qualitative agreement being obtained throughout. However, this agreement is still not quantitative, with the calculations deviating significantly outside of the present errors at around $\theta \approx 60°$ and $\theta \geqslant 110°$ or at small θ. The UFOMBT is observed to overestimate the magnitude of the forward-scattering DCS's at all $E_0 \geqslant 40$ eV.

At $E_0 = 50$ eV and 100 eV we observe significantly improved agreement with the perturbative models, especially the UFOMBT. The UFOMBT provides very good quantitative agreement, deviating from the present DCS's only over a small range of angles at $E_0 = 50$ eV [Fig. 5(e)] and 100 eV [Fig. 5(f)]. Interestingly, the SCGS-RDWA does somewhat better than the MCGS-RDWA, although an average of the two would produce excellent agreement with experiment. Both the CV3-15-DWBA and HF-DWBA are in very good qualitative agreement with experiment and little difference is observed between them, although they use different codes to generate their wave functions. At $E_0 = 50$ eV and 100 eV, the present DCS's are in excellent agreement with the values of Register *et al.* [8], with perfect agreement at 50 eV and 1 point at $\theta = 100°$ deviating away from the UFOMBT and the present results. However, Register *et al.*'s 100 eV DCS's represent the $(2p^53s)[1/2]^\circ_1$ DCS's alone, since the other levels are not included in their paper. When only the individual $(2p^53s)[1/2]^\circ_1$ DCS's are compared [in Fig. 9(d), later] the agreement between the experimental values is perfect.

B. Individual $2p^53s$ level DCS's

The individual DCS's are only shown graphically at select E_0 values of 20, 30, 50, and 100 eV. At $E_0 = 20$ eV [Figs. 6(a)–6(d)], which is where the *R*-matrix should provide the best agreement, we observe significant disagreements, for all levels. For example, the $(2p^53s)[3/2]^\circ_2$ DCS's [Fig. 6(a)] are significantly greater than those from the model at intermediate θ, around 50°. The rapid rise in the DCS's for excitation of the $J = 1$ levels [Figs. 6(b) and 6(d)] at small θ is also not observed in the theory. While the model fits the large

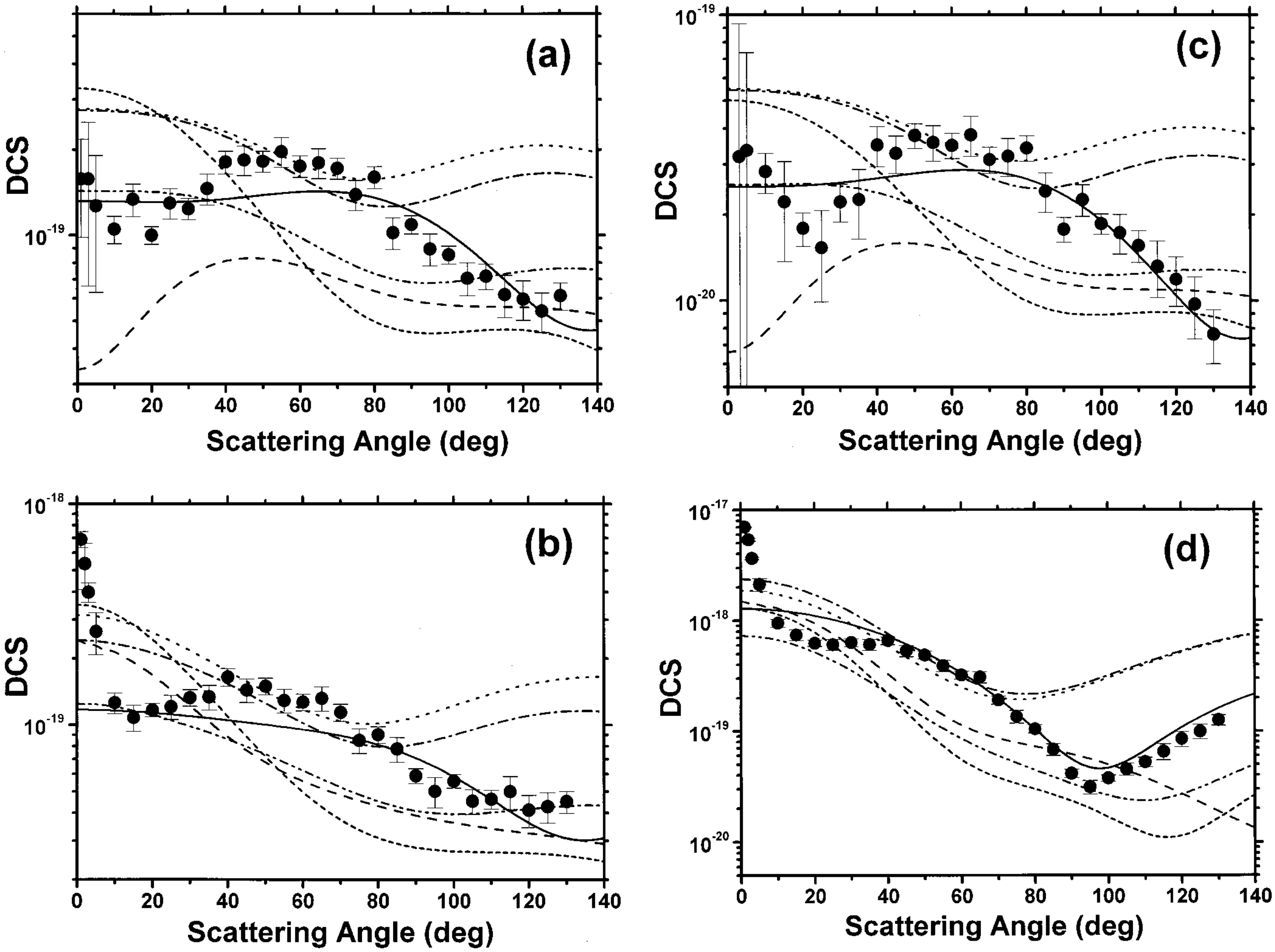

FIG. 6. DCS's for the electron impact excitation of the individual levels comprising the $2p^53s$ configuration of Ne at $E_0=20$ eV. See also Table II(a). Experiments: ●, present data with error bars. Theories:—, R-matrix method; – – –, UFOMBT; — - —, CIV3-15-DWBA; - - -, HF-DWBA; – – –, SCGS-RDWA; - - -, MCGS-RDWA. (a) $(2p^53s)[3/2]^\circ_2$ feature, (b) $(2p^53s)[3/2]^\circ_1$ feature, (c) $(2p^53s)[1/2]^\circ_0$ feature, and (d) $(2p^53s)[1/2]^\circ_1$ feature. See text for discussion.

angle DCS's of the $(2p^53s)[1/2]^\circ_1$ level ($\theta > 70°$), it does not do this for the other $J=1$ level $[(2p^53s)[3/2]^\circ_1]$. In Fig. 6(c), there is some evidence of a dip in the DCS of the $(2p^53s)[1/2]^\circ_0$ at $\theta = 20°$ which is also not evidenced by the theory. This observation is discussed further in our conclusions in Sec. V. At this low E_0 value, the UFOMBT, DWBA, and RDWA models do not show any consistent agreement with the experiment.

At $E_0=30$ eV [Figs. 7(a)–7(d)] the situation remains similar to that at 25 eV, except for the $(2p^53s)[3/2]^\circ_1$ level [Fig. 7(b)] where we observe that the UFOMBT gives very good agreement, in contrast to the R-matrix. The situation reverses for $(2p^53s)[1/2]^\circ_1$ [Fig. 7(d)], where the R-matrix provides a better result, whereas the UFOMBT produces a curve similar to that for the $(2p^53s)[3/2]^\circ_1$ excitation.

At $E_0=50$ eV [Figs. 8(a)–8(d)] agreement between the two experiments for all individual DCS's is excellent. In Figs. 8(a) and 8(c) the experimental DCS's show a dip toward small θ. The DWBA, RDWA, and UFOMBT reproduces the dip for both these forbidden levels. We suspect however that a systematic problem manifests itself in these dips since they are not present at $E_0=100$ eV; cf. next paragraph. At small θ, the $J=0$ feature is dwarfed by the nearby $J=1$ features. This potential systematic problem is further discussed in Sec. V (conclusions).

At $E_0=100$ eV [Figs. 9(a)–9(d)] very good agreement between the UFOMBT and the experimental values is found only for the DCS for excitation of the $(2p^53s)[1/2]^\circ_1$ level [Fig. 9(d)], for which both experimental sets agree mostly within error bars. The small-θ drop in the DCS's of the $J=2$ and $J=0$ levels [Figs. 9(a) and 9(c)] is very clear at this E_0, but no dip develops. The models do not reproduce the minimum in the DCS at $\theta = 55°$ for the $(2p^53s)[3/2]^\circ_2$ level [Fig. 9(a)] and washes over the oscillatory structure in the DCS at large θ. The UFOMBT shows almost perfect agreement with the Register *et al.* [8] DCS's and at small θ. The present DCS's are lower than the Register *et al.* DCS's and the UFOMBT. For the $(2p^53s)[3/2]^\circ_1$ excitation, agreement with the present DCS's is significantly worse, with the theory overestimating the DCS at $\theta \leqslant 80°$.

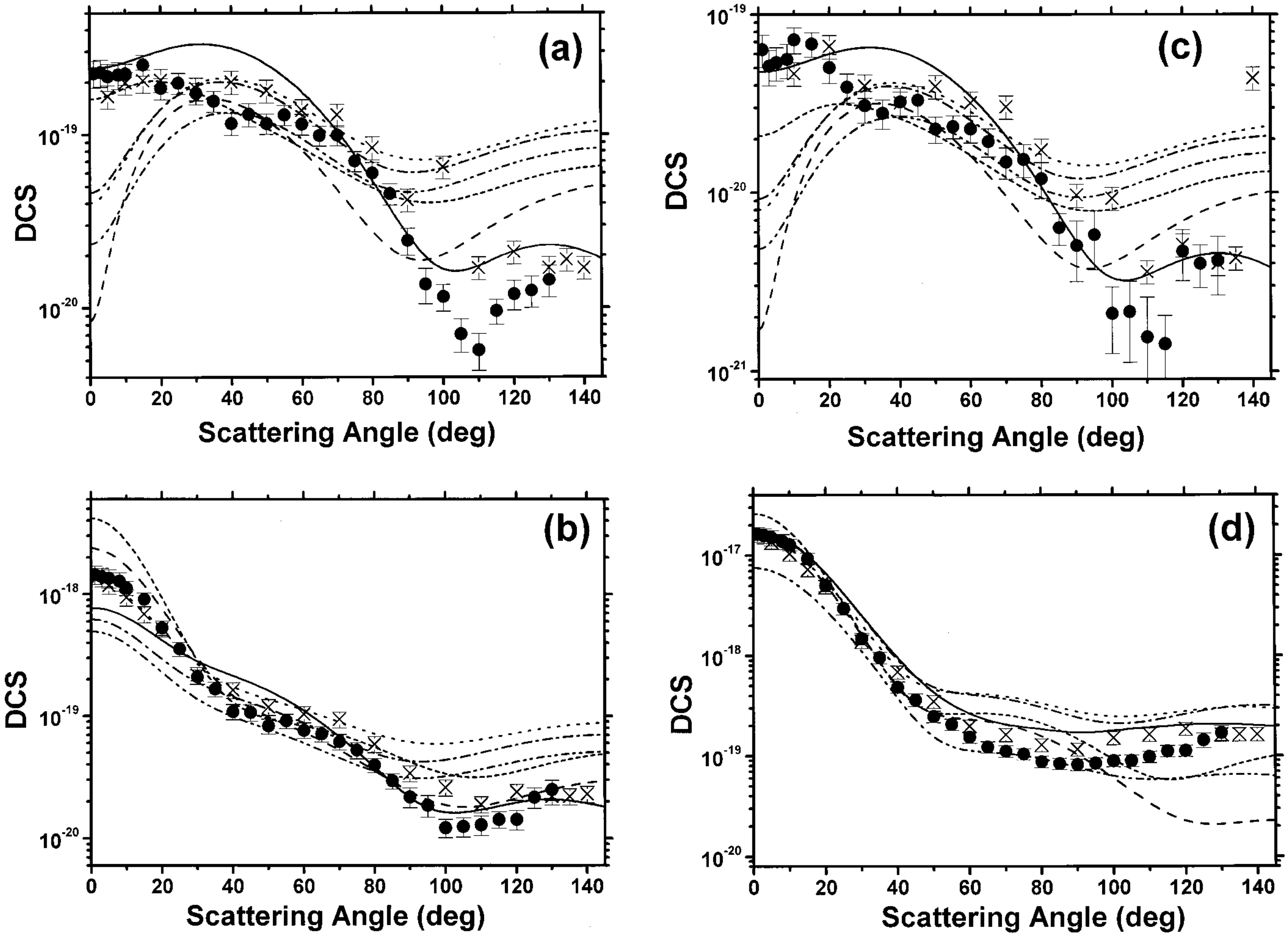

FIG. 7. Same as Fig. 6, but for $E_0 = 30$ eV. Experiment: ×, Register *et al.* [8]. See also Table II(c) and text for discussion.

C. Integral cross sections

The integral cross sections (ICS) are shown in Figs. 10(a) and 10(b) for the $(2p^5 3s)[3/2]^\circ_1$ and $(2p^5 3s)[1/2]^\circ_1$ levels, respectively. Comparison with the ICS's of Register *et al.* [8] is also given. The errors in our ICS's include errors induced in the extrapolation of the DCS's to large θ. These ICS's were used to renormalize the excitation functions measured by Kanik *et al.* [17] also shown in these figures. The ICS's for all excitations are tabulated in Table IV. The excitation function for the $(2p^5 3s)[1/2]^\circ_1$ level [17] (744 nm) was multiplied by 1.20 whereas for the excitation function for the $(2p^5 3s)[3/2]^\circ_1$ level (736 nm) this factor was 0.45. This difference in the normalization factor is interesting because the emission measurements were originally normalized to the Born approximation at high E_0 using the optical oscillator strength (OOS) for the $(2p^5 3s)[1/2]^\circ_1$ excitation. This is not due to detection efficiency of the apparatus used by Kanik *et al.* [17], since the wavelengths of these transitions are very close together and therefore their quantum efficiency should be similar. In any case, the detection efficiency of their apparatus was corrected for its wavelength dependence. It is therefore more likely due to the effects of cascade because the $(2p^5 3s)[3/2]^\circ_1$ has a triplet nature and thus has a different and probably greater cascade contribution.

D. DCS ratios

In Figs. 11–14, the ratios of Register *et al.* [8] and now the present data measurements show excellent agreement. Figures 11(a)–11(c) show the ratios r, r', and r'' at $E_0 = 20$ eV. We observe [Fig. 11(a)] that r stays close to the statistical value of 5. The region around $75° \leqslant \theta \leqslant 120°$ shows lower values of r. However, the average of the data in this region yields $r = 4.63 \pm 0.56$ (standard deviation on the mean) which still overlaps the $r = 5$ line. We note the significantly larger r values at small θ predicted by the MCGS-RDWA of 6.53. At such small θ increased values of r are also observed at other E_0 (see following text). The experimental r' ratio shows a large rise around $\theta = 90°$ which is qualitatively reproduced by the R-matrix model, but not by the perturbative methods. A rise in the r' ratio indicates the effect of exciting the $|^3P\rangle$ component of the $J = 1$ levels [see Sec. I, Eqs. (3) and (4)]. Comparison amongst the calculations demonstrates the ability of the R-matrix to model the (spin-exchange) related scattering dynamics at low energy, whereas the UFOMBT, DWBA, and RDWA are unable to do this. We also note that the fall in r' observed experimentally for $\theta < 5°$ is not reproduced by any of the theories. The experimental $\theta \to 0$ intercept of r' is 0.086 ± 0.007. These

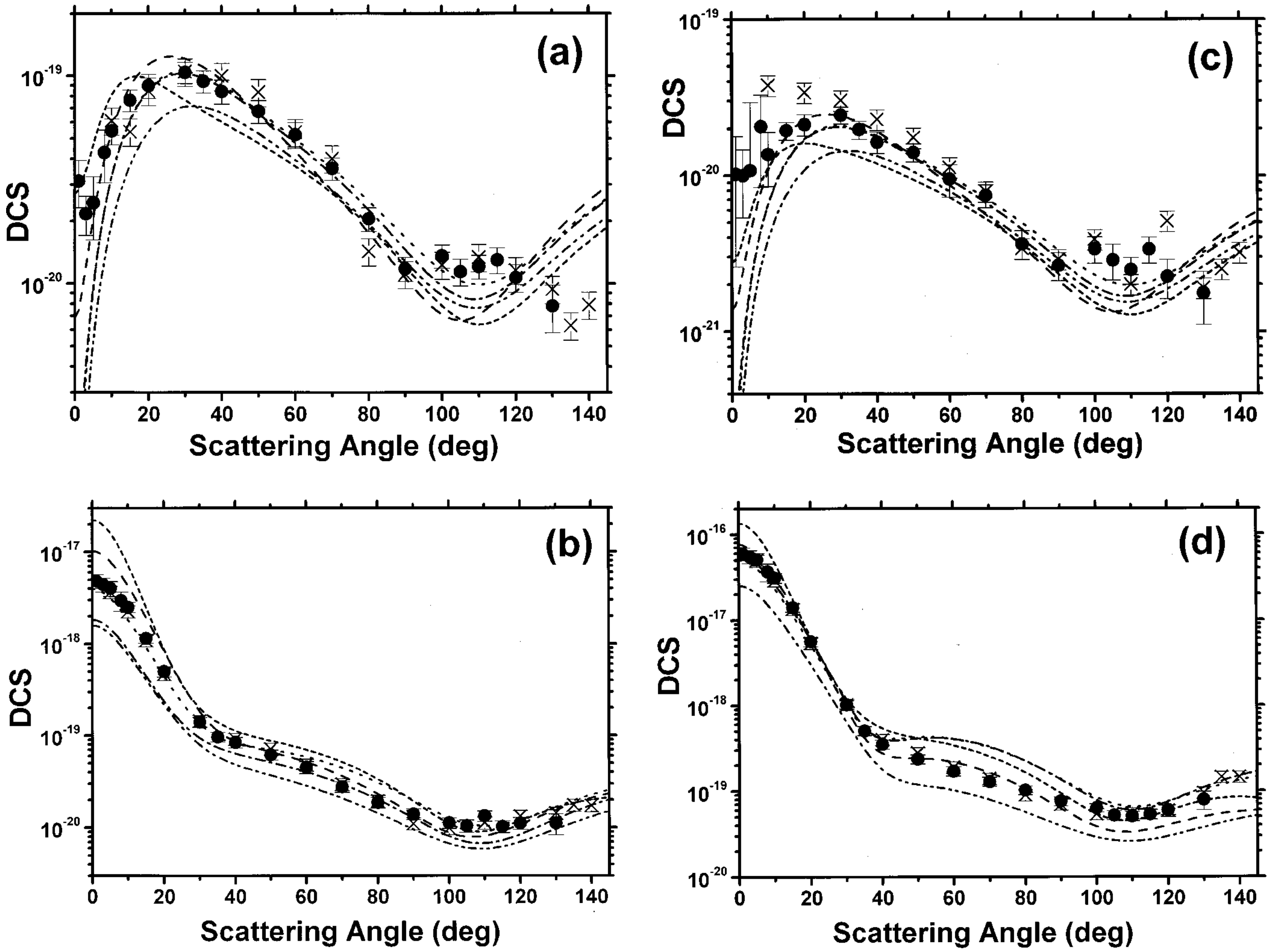

FIG. 8. Same as Figs. 6 and 7, but for $E_0 = 50$ eV. See also Table II(e) and text for discussion.

$\theta \rightarrow 0$ values are summarized in Fig. 15. The *R*-matrix, the DWBA, and the RDWA give good, qualitative agreement with the present r'' ratio parameters [Fig. 11(c)] at low θ, but the UFOMBT shows significantly lower r'' values in this region.

At $E_0 = 30$ eV [Fig. 12(a)], it is clear that the r parameter stays significantly below the statistical weight value of 5 at small $\theta < 30°$, however these small $\theta < 30°$ r values give an average r of 4.7 ± 1.6, which is again within the r value of 5. In Fig. 12(b), the r' values from both experiments and those of an earlier experimental investigation by us (Khakoo *et al.* [1]) are in excellent agreement showing a very clear r' vs θ curve. Agreement with all models is unsatisfactory, and although the *R*-matrix shows good qualitative agreement, i.e., returning to low r' values below $\theta > 90°$, it does not achieve the high experimental r' value of 0.59 ± 0.03 at $\theta = 60°$. Our ($\theta \rightarrow 0°$) r' ratio is 0.089 ± 0.001 [Fig. 12(b)] in (severe) disagreement with all models except the HF-DWBA which uses the experimental α and β parameters. In Fig. 12(c), we observe very much improved r'' values from the models at small θ. However, the *R*-matrix values are larger than the experimental r'' values at small θ which are in good agreement with the perturbative methods at these angles.

At $E_0 = 50$ eV [Fig. 13(a)] we observe r values again close to 5, but note that the Register *et al.* [8] values dip to low values at small θ. This effect is again due to systematic problems associated with the unfolding of the $J = 0$ feature from the spectra at small θ from the overshadowing (nearby), intense $J = 1$ features. This problem is reduced in the present analysis which uses more accurate instrumental line shapes [derived from the $(2p^5 3s)[1/2]^\circ_1$ feature] as compared to Register *et al.* [8] (using the elastic scattering peak). For r' [Fig. 13(b)] reasonable qualitative agreement between the models and experiments is observed, but there is some significant scatter between the models and we note again the differences at small θ between the experiments (which agree excellently) and the models. The UFOMBT and the MCGS-RDWA remain higher than the experiments, whereas the SCGS-RDWA shows a low r' value. Excellent agreement between the experiments is observed in the calculations for the r'' parameter, which displays a double-hump structure [Fig. 13(c)]. However, this structure is barely observed in the calculations and is shown only by the RDWA and the DWBA models. At small θ values there is good agreement with experiment, but they deviate for $\theta > 50°$.

Finally at $E_0 = 100$ eV, it is hard to determine r with small uncertainties because of the difficulty in getting good

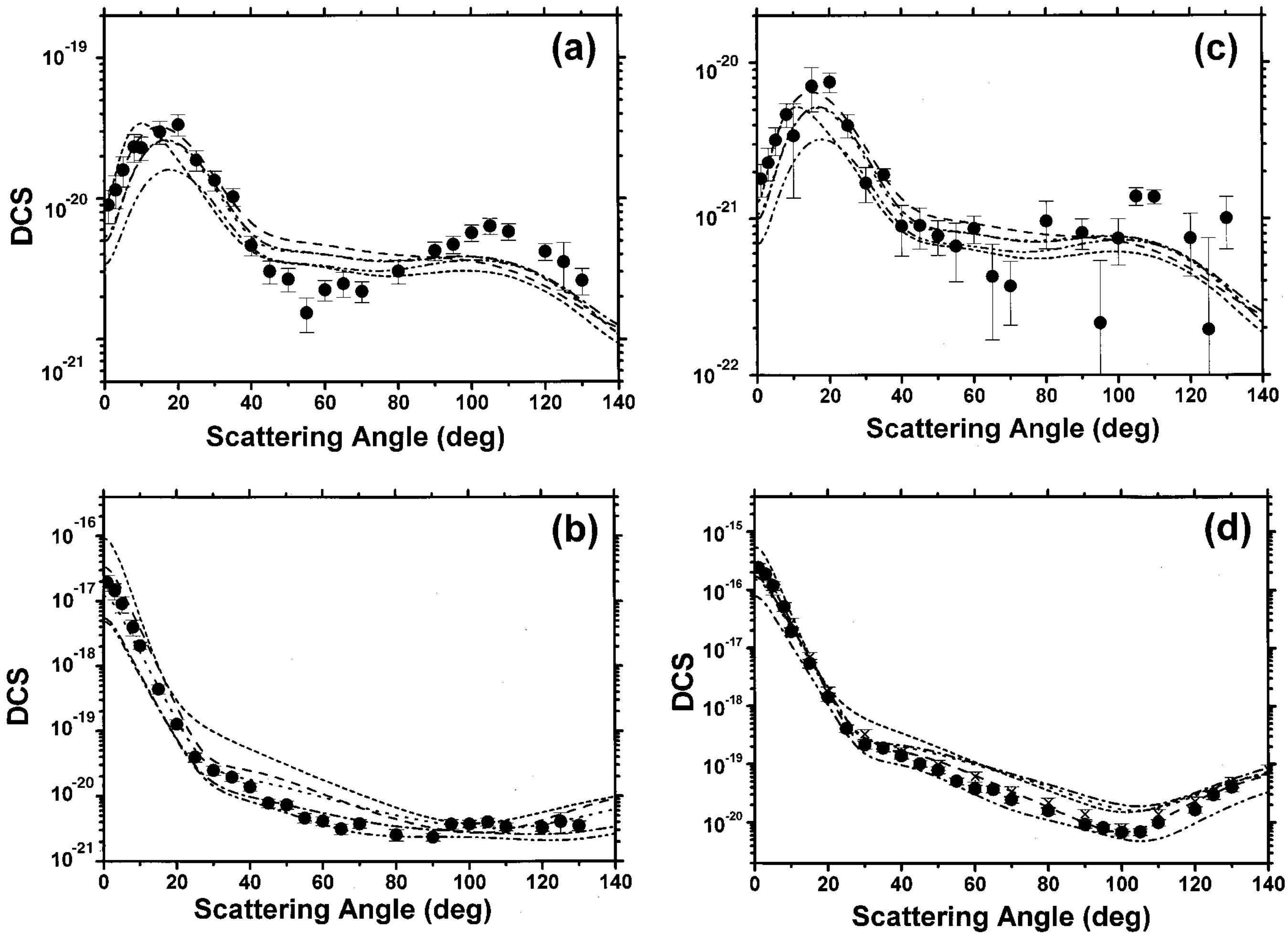

FIG. 9. Same as Figs. 6 and 7, but for $E_0 = 100$ eV. See also Table II(f) and text for discussion.

counting statistics for the $J = 0$, 2 features. However, we see r staying on average around the statistical weight value of 5 [Fig. 14(a)]. For r', we observe two peaks of which even the weak peak at $\theta = 30°$ is observed in the UFOMBT data. The more prominent peak experimentally observed at $\theta = 105°$, is sharper than the theoretical one [Fig. 14(b)]. The r' value at 105° is 0.62 and again shows the increased spin-exchange in this region. The r' $\theta \rightarrow 0$ limit is observed experimentally to be 0.079 ± 0.001 and this remains in disagreement with the UFOMBT value of 0.136, the MCGS-RDWA value of 0.169 and the SCGS-RDWA value of 0.062, but in agreement with the HF-DWBA value of 0.082 and CIV3-15-DWBA value of 0.077. We also note the present experimental value is in very good agreement with the experimental optical oscillator strength ratios of Chan *et al.* [39] of 0.0742 ± 0.0053 (Table V). In Fig. 14(c), all the models except the MCGS-RDWA give excellent qualitative agreement with experiment, showing the minor peak at around $\theta = 30°$.

To summarize these ratio results, we note that r remains around its statistical weight value of 5 for all E_0 and θ. The MCGS-RDWA model shows small θ values of $r > 5$, especially at the higher E_0 values. Comparing at small θ, r' values obtained by the different theoretical models we see from the R-matrix (at $E_0 = 30$ eV; the highest energy it could be reasonably applied) that we get a value of 0.046. At $E_0 = 100$ eV the UFOMBT gives 0.131, the CIV3-15-DWBA gives 0.033, the HF-DWBA gives 0.077, the SCGS-RDWA gives 0.063 and the MCGS-RDWA gives 0.171. These r' values are directly the ratio of the optical oscillator strengths for the $(2p^5 3s)[3/2]^\circ_1$ and $(2p^5 3s)[1/2]^\circ_1$ levels. This clearly indicates several important facts.

(i) The intermediate-coupling coefficients computed from the Cowan code (used by the UFOMBT) as well as those computed by the CIV3 code (used by the DWBA) are found to be the most inaccurate. A more accurate calculation of these numbers would significantly improve agreement, specifically for r' at small θ.

(ii) Variation in β, i.e., that of the minor coefficient, affects r more strongly than α. Thus the inclusion of the ${}^3P$ levels to the correct amount in the intermediate coupling expansion is important in converging to a more quantitatively correct model.

(iii) From the results of the DWBA we see that the use of Hartree-Fock or CIV3 wave functions makes little impact on the model results, indicating that the intermediate coupling coefficients provide important guides to obtaining agreement with experiment.

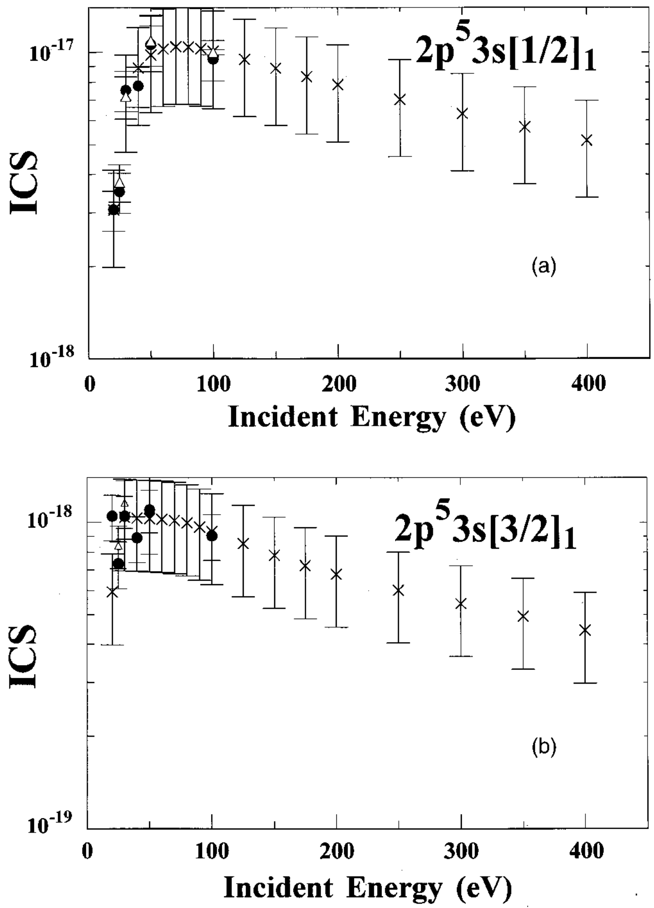

FIG. 10. Integral cross sections for the optically allowed resonance transitions of Ne. (a) $(2p^53s)[1/2]^\circ_1$ feature and (b) $(2p^53s)[3/2]^\circ_1$ feature. Experiments: ●, present data with error bars; △, Register *et al.* [8]; ×, Kanik *et al.* [17] (optical emission measurements). The error bars in the emission measurements include a 22% relative intensity error plus the error on the normalization to our ICS's [15% for (a) and 17% for (b)].

(iv) From the RDWA results we observe, in general, that the SCGS results give a better small θ agreement with experiments. This could be a measure of the way that the multiconfiguration is put together to provide agreement with the energy level values, but using these ratios a better method could be achieved.

Considering that this is the simplest rare gas target with an np^6 ground state configuration, it is important for new models to eliminate many of the differences between experiments and the present models, before any progress can be made in electron-rare gas collisions. The ratios clearly point out important aspects of the theoretical approaches which could be improved so that this may be achieved.

E. Optical oscillator strength extrapolations

From a plot of r' vs E_0 (Fig. 15) one could expect that the dipole limit of r' at $\theta=0°$ is reached at $E_0=100$ eV, but clearly not at 50 eV. To test this we have used the small angle DCS's for excitation of the $(2p^53s)[1/2]^\circ_1$ level from the experimental results and the UFOMBT at $E_0=50$ eV and 100 eV, which are in excellent agreement at these energies (see Figs. 8 and 9). These DCS's were converted into apparent generalized oscillator strengths (AGOS), χ_{AGOS}, using the formula [40]

$$\chi_{\mathrm{AGOS}}(E_0,\theta)=1/2\,\Delta E\,k_0/k_nK^2\sigma(E_0,\theta), \qquad (10)$$

where ΔE is the energy-loss (in a.u.), k_0, k_n are the incident and scattered electron momenta (a.u.) and $K^2[=k_0{}^2+k_n{}^2-2k_0k_n\cos(\theta)]$ is the momentum transferred to the atom by the scattered electron. The AGOS were extrapolated to the $K^2=0$ limit by the polynomial (based on the validity of the Born approximation in this regime) [41]:

$$\chi_{\mathrm{AGOS}}=\frac{1}{(1+x)^6}\sum_{m=0,1,2}C_m\frac{x^m}{(1+x)^m}. \qquad (11)$$

In Eq. (11), $x=K^2/\Lambda^2$ and $\Lambda=[2I]^{1/2}+[2|I-\Delta E|]^{1/2}$, where I is the ionization energy in a.u. In the limit of $K^2=0$, AGOS→OOS$(=C_0)$. The AGOS values of our experiment and those of the UFOMBT at 100 eV are shown extrapolated to the $K^2=0$ limit in Fig. 16. We note that the extrapolated value of the OOS at $E_0=100$ eV of 0.172 ± 0.001 significantly exceeds the dipole(*e*,*e*) OOS values (see Table V) and thus show that the Born limit is not yet realized at $E_0=100$ eV. A similar procedure at $E_0=50$ eV gives an even higher extrapolated OOS value of 0.193 ± 0.014, with increased uncertainties, demonstrating that it is not possible to reliably extrapolate to the OOS at any energy below the Born region. It also shows that the dipole limit of r' is reached at significantly lower E_0 values than the Born limit.

TABLE IV. Integral cross sections with corresponding uncertainties (1 standard deviation) for the individual $2p^53s$ excitations of Ne obtained by angle integrating the measured DCS's.

E_0(eV)	$2p^53s$	$2p^53s[3/2]_2^\circ$	$2p^53s[3/2]_1^\circ$	$2p^53s[1/2]_0^\circ$	$2p^53s[1/2]_1^\circ$
20	58.5 +/− 6.9	14.6 +/− 3.2	10.5 +/− 1.8	2.7 +/− 0.7	30.7 +/− 4.6
25	52.2 +/− 6.3	8.0 +/− 1.6	7.4 +/− 1.3	1.7 +/− 0.4	35.2 +/− 5.3
30	95.5 +/− 12.0	9.7 +/− 1.7	10.5 +/− 1.7	1.7 +/− 0.4	75.4 +/− 11.3
40	92.8 +/− 11.0	4.9 +/− 1.0	8.9 +/− 1.5	1.1 +/− 0.3	77.9 +/− 11.7
50	122.1 +/− 16.4	4.0 +/− 0.8	11.0 +/− 1.8	0.9 +/− 0.2	106.2 +/− 15.9
100	105.0 +/− 13.8	0.6 +/− 0.2	9.1 +/− 1.5	0.1 +/− 0.0	95.2 +/− 14.3

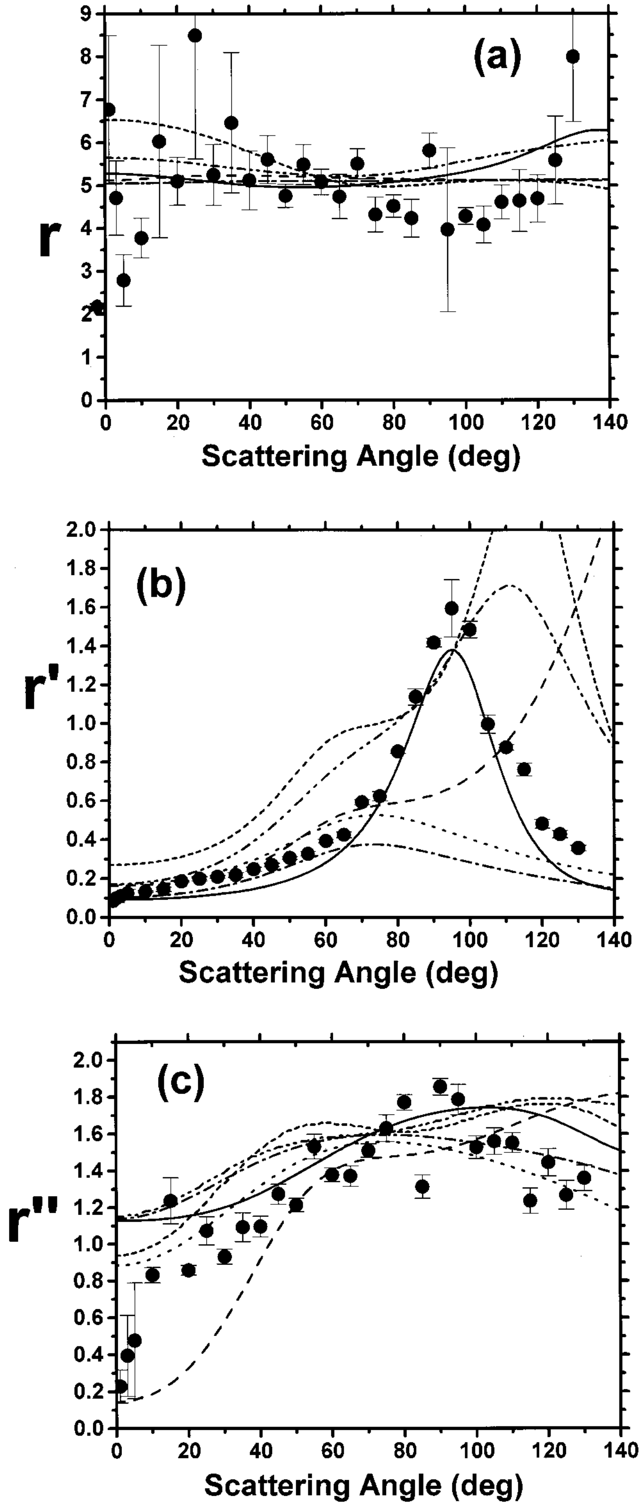

FIG. 11. Differential cross-section ratios r, r', and r'' for Ne at $E_0 = 20$ eV. See also Table II(a). Experiments: ●, present data with error bars; theories: –, *R*-matrix method; – – –, UFOMBT; — - —, CIV3-15-DWBA; - - -, HF-DWBA; — - - —, SCGS-RDWA; - - -, MCGS-RDWA. (a) r, (b) r', and (c)r''. See text for discussion.

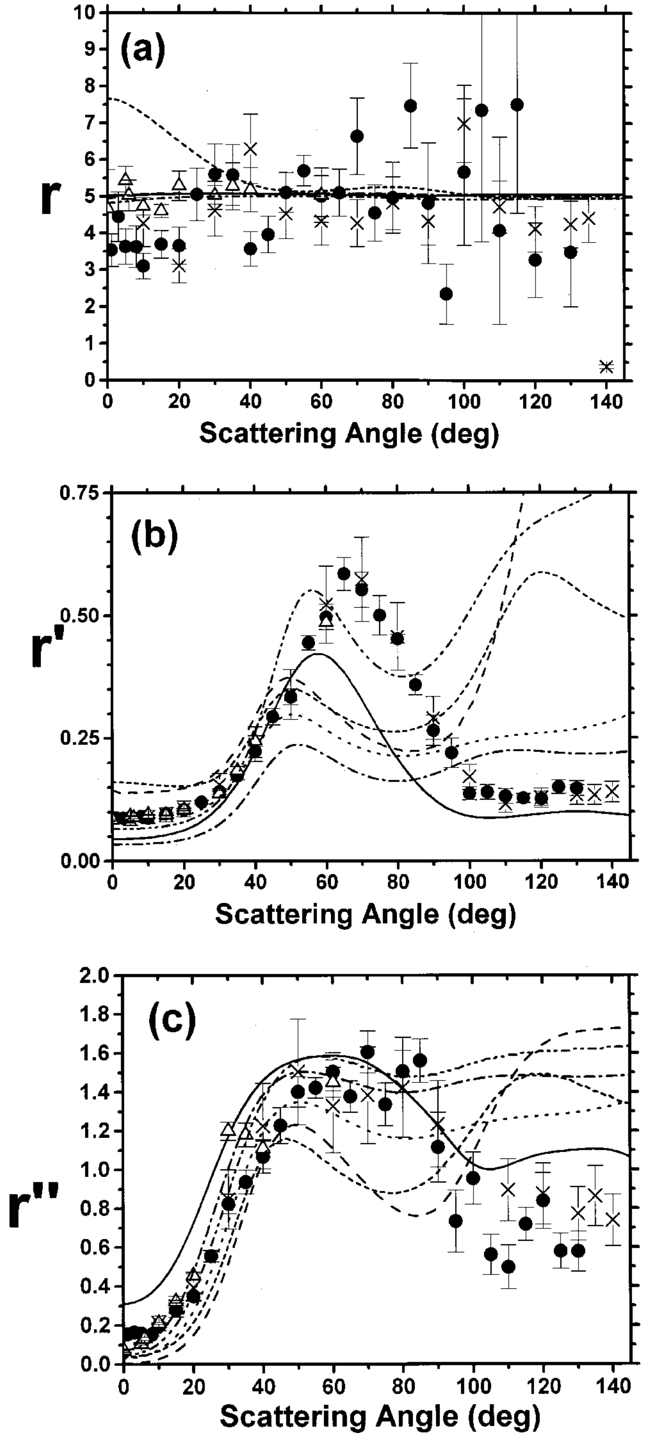

FIG. 12. Same as Fig. 11, but at $E_0 = 30$ eV. See also Table II(c). Experiments: ×, Register *et al.* [8]. (a) r, (b) r', and (c) r''. See text for discussion.

V. CONCLUSIONS

We make several conclusions in this work.

First, that it is feasible to use the method of mixtures to great advantage in determining accurate experimental DCS's.

Determining r with small uncertainties (to the same ex-

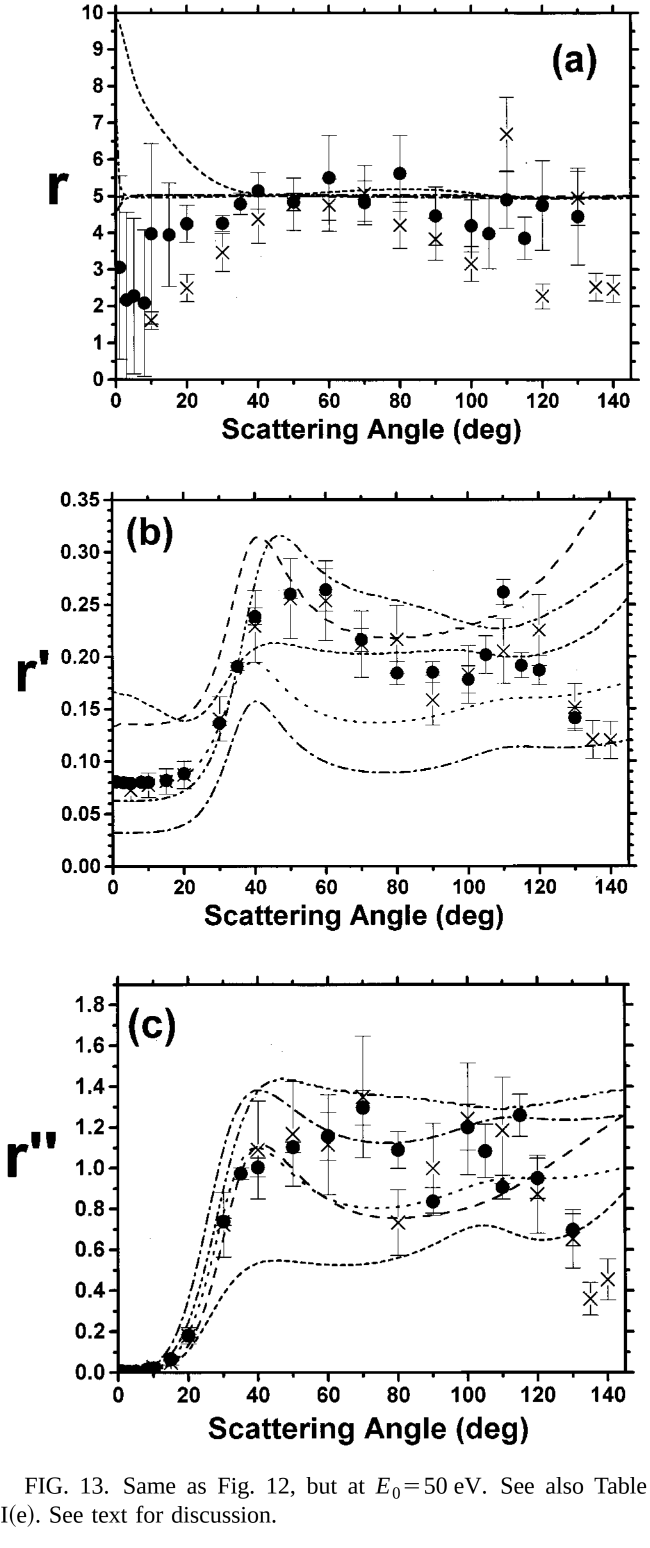

FIG. 13. Same as Fig. 12, but at $E_0 = 50$ eV. See also Table II(e). See text for discussion.

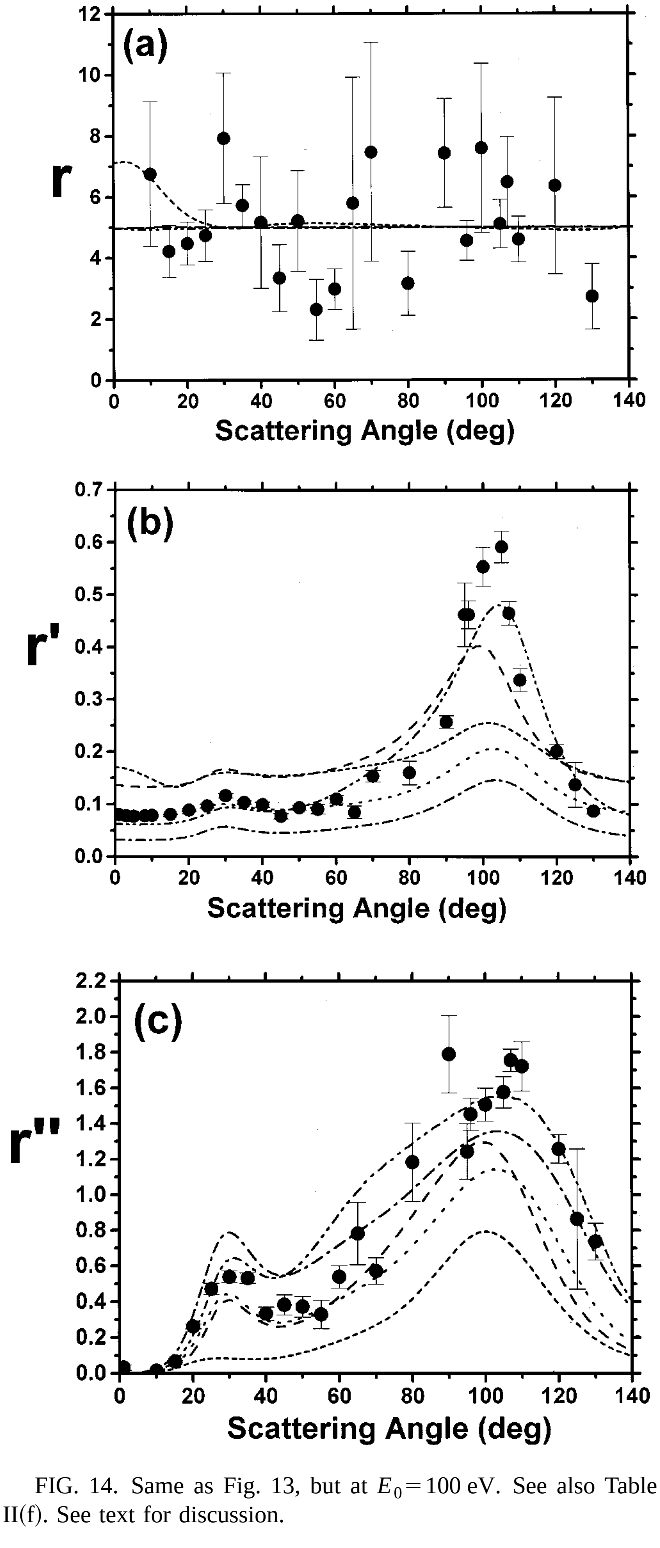

FIG. 14. Same as Fig. 13, but at $E_0 = 100$ eV. See also Table II(f). See text for discussion.

treme as r' or r'') is difficult because of the weak $(2p^5 3s) \times [1/2]^\circ_0$ level's DCS's. However, this is an interesting parameter to know since a breakdown of the $r = 5$ statistical law indicates that spin-orbit effects are prevalent in the collision dynamics, which describe the excitation of the forbidden levels. Presently, we are considering making electron-metastable coincidence measurements in an effort to reduce these uncertainties.

We next note that the r' parameter clearly shows that target structure is not well represented in the existing models and that progress towards a better representation must be made before one can expect agreement between theory and experiments. The r' parameter can be used to great effect in choosing the quantitative form of wave functions so that correct modeling can be achieved.

The r'' parameter complements the r' parameter in that it

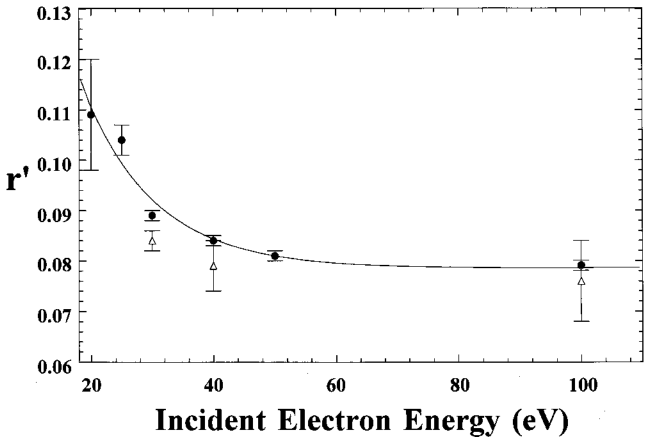

FIG. 15. r' $(\theta=0)$ values as a function of E_0. ●, present data with error bars; △, Khakoo *et al.* [1]. The line is a nonlinear least squares fit to the present results using an exponential-type function.

shows excitation strength of the metastable excitation channels relative to the allowed channels. In most cases, r'' is not satisfactorily calculated in the present models.

In addition, the results for the individual DCS's for the $2p^5 3s$ configuration levels show substantial differences between the various theoretical approximations. At the highest energy shown ($E_0 = 100$ eV) the distorted-wave theories are in reasonable agreement with each other and with experiment. This is expected since these theories become more accurate as the energy increases. However, at lower energies the differences are much larger. It is clearer that in the case of Ne, the results are very sensitive to the method used and to the wave functions used to represent the excited states of the atom. The best indication of the sensitivity to the wave functions is the difference between the HF-DWBA and the CIV3-15-DWBA results. These were identical except for the wave functions used. It is also disappointing that there is a lack of convergence between the *R*-matrix and DWBA results using the same wave functions even at $E_0 = 30$ eV, the highest energy for which the *R*-matrix results are shown. Further work is needed in order to obtain reliable theoretical results in the intermediate energy range.

Perhaps Ar would be a better case to test the agreement between theory and experiment. Previous calculations have shown much more consistency between the RDWA and DWBA results [46,51,52] for this target. Experimental work on Ar is ongoing and we intend to present a detailed comparison between theory and experiment for this gas as well in the near future.

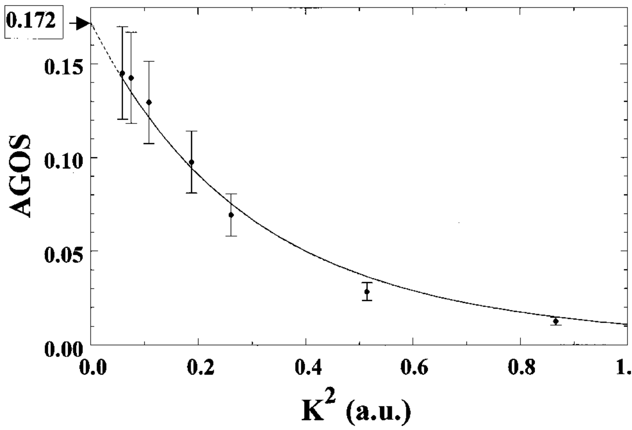

FIG. 16. Optical oscillator strength extrapolation of the apparent generalized oscillator strength at $E_0 = 100$ eV for the $(2p^5 3s) \times [1/2]^{\circ}_1$ feature using Vriens' [41] polynomial [Eq. (11)]. The dashed line section of the fit is the extrapolated fit. See text for discussion.

Also, in the case of the experiment we require more precise values of the ratio *r* to investigate the role of spin-orbit effects in the scattering. In this case a better experimental method which could be used is that of electron-metastable coincidence. This method should provide improved statistics and consequently improved data. It is also applicable to all the rare gases. This approach is currently also being considered experimentally.

ACKNOWLEDGMENTS

This work was funded by the National Science Foundation under Grants No. RUI-PHY-9731890 (M.A.K), PHY-0070872 (D.H.M), and PHY-0088917 (K.B.). R.S. is grateful to the Department of Atomic Energy, Government of India for financial support. A.D.S. wishes to thank the Natural Sciences and Engineering Research Council of Canada for a grant in aid of this research. M.A.K thanks H. Fabris and D. Parsons for expert technical support and acknowledges undergraduates Gary Mikaelian and Gil Vitug for the angular profile measurements of the mixed gases used in the Appendix. Discussions with Professor T. J. Gay (University of Nebraska, Lincoln) and with Professor J. F. Williams

TABLE V. Recent experimental OOS derived values (with corresponding uncertainties) of r' for Ne and the consequent α, β parameters (and uncertainties) determined from these. See text for discussion. See Ref. [39] for a full summary of optical measurements.

$2p^5 3s[3/2]_1^{\circ}$	$2p^5 3s[1/2]_1^{\circ}$	r'	Ref.	Method	α	β
		0.0785 +/− *0.0029*	Present	Electron energy loss	0.963 +/− 0.001	0.270 +/− 0.005
0.0118 +/− *0.0006*	0.159 +/− *0.008*	0.0742 +/− *0.0053*	[39]	High resolution dipole (e,e)	0.965 +/− 0.002	0.263 +/− 0.009
0.0122 +/− *0.0006*	0.123 +/− *0.006*	0.0992 +/− *0.0069*	[42]	Absolute self-absorption	0.954 +/− 0.003	0.300 +/− 0.009
0.0120 +/− *0.0030*	0.144 +/− *0.024*	0.0833 +/− *0.0250*	[43]	Total absorption	0.961 +/− 0.011	0.277 +/− 0.038
0.0109 +/− *0.0008*	0.147 +/− *0.012*	0.0741 +/− *0.0081*	[44]	Absolute self-absorption	0.965 +/− 0.004	0.263 +/− 0.013
0.0122 +/− *0.0009*	0.148 +/− *0.014*	0.0824 +/− *0.0099*	[45]	Hanle effect lifetime	0.961 +/− 0.004	0.275 +/− 0.015

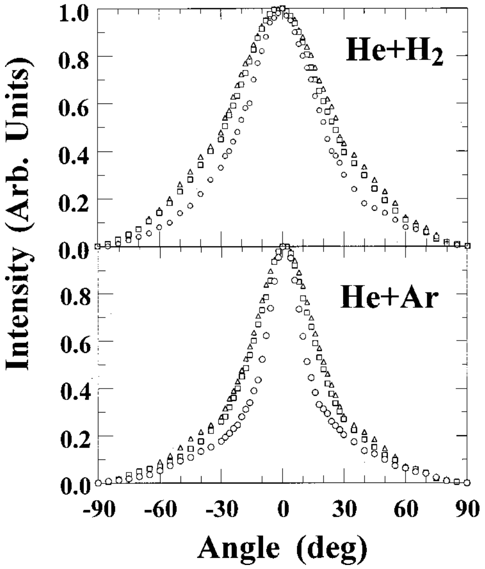

FIG. 17. (a) Gas beam profiles for He+H$_2$ taken for a 20 mm long, 0.8 mm diameter needle with the gases led through individually or gases mixed. (b) Same as (a), but for He+Ne. (c) Same as (a), but for He+Ar. He (open circles); He with the gas (open squares); gas with He (open triangles).

(University of Western Australia, Perth) are gratefully acknowledged.

APPENDIX: METHOD OF MIXTURES

By introducing the two gases as a mixture, intergas collisions broadening should make the particles emerging out of the collimating tube to have essentially the same angular profiles. Rugamas *et al.* [47] have shown experimentally that the angular profiles of gases emanating out of a collimating tube, for a wide range of gases, is essentially dependent on the mean-free path, λ, of the gas given by [48]

$$\lambda = \frac{1}{\sqrt{2} n \pi \delta^2}. \tag{A1}$$

This observation, although not strictly correct, is accurate to an experimental uncertaintly of ≈6%. This observation also supports the theoretical considerations of Olander and coworkers [49]. In Eq. (A1), δ is the molecular diameter of the gas which is related to its kinetic cross section, σ, by ($\sigma = \pi\delta^2$; δ is the molecular diameter of the gas) and n is the average number density of the gas in the source. In this case for a tenuous gas, the ideal gas equation applies and $n = P/kT$, where P is the pressure of gas in the source reservoir, k is Boltzmann's constant, and T is the temperature of the gas. However, given a mixture of gases a and b the mean-free paths for these gases is given (for a and b) as

$$\lambda_a = \frac{1}{\sqrt{2}(n_a\sigma_{aa} + n_b\sigma_{ab})}, \quad \lambda_b = \frac{1}{\sqrt{2}(n_b\sigma_{bb} + n_a\sigma_{ab})}, \tag{A2}$$

where n_a and n_b are the number densities of the two gases, σ_{aa}, σ_{bb} are the collision cross-sections of gas a and gas b with itself, whereas σ_{ab} is the intergas a and b collision cross-section. Since the second terms in the denominator in Eq. (A2) are different $\lambda_a \neq \lambda_b$. This implies that the gas profiles of the constituents of the mixture should differ. However, Eq. (A2) does not take into account the dynamic broadening of gas a by b in terms of the details of the collision process, and e.g. does not consider the effect of mass.

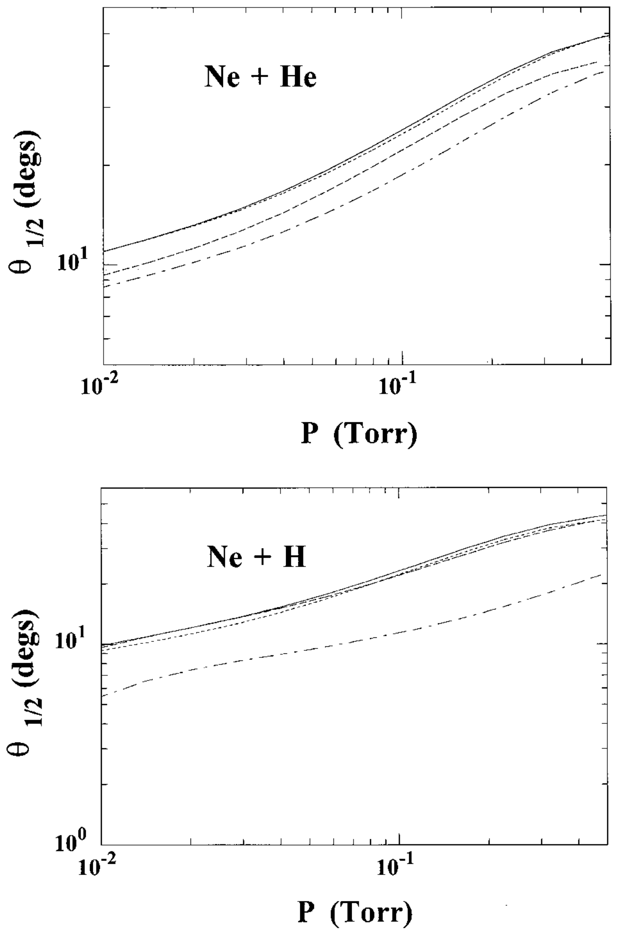

FIG. 18. Results of model using collision mean-free path analysis to numerically obtain the FWHM profiles of mixed and unmixed gases. In this case (a) He and Ne and (b) Ne and H. FWHM profiles of mixed (solid line, small dashes) and unmixed (medium dashes; long dash-short dash) gases. The heavier gas has the larger FWHM.

To investigate the above we have taken measurements of gas beam profiles for different mixtures of H$_2$/He/Ne/Ar/Xe. The profiles were taken using a mass-sensitive gas beam sensor (with the simple Bayert-Alpert ionization gauge sensor in the work of Rugamas *et al.* [47] replaced by a quadrupole minimass spectrometer). These measurements showed that the profiles of the constituent gases were closely similar, even when the profiles of the separated, unmixed gases were not similar. A sample of such profiles is shown in Fig. 17.

In an attempt to understand the experimental results, which contradict Eq. (A2), we remodeled our mean-free path hypothesis to include the effect of interatom collisions to the gas beam profile in the following way.

(i) First, the universal curve for the experimental gas beam profiles in Rugamas *et al.* [47] for the single tube (diameter 0.8 mm and length 20 mm) was obtained via a polynomial least-squares fit to their profiles as a function of mean-free path to obtain the equation

$$\theta_{1/2}=8.32944126-0.64003071\lambda+1.73717355\lambda^{-1}-0.031817351\lambda^{-2}+0.00020997886\lambda^{-3}, \qquad (A3)$$

where $\theta_{1/2}$ (deg) is the full width at half maximum of the profile for the mean-free path of the gas λ (cm). [Note: the polynomial expansion in Eq. (A3) is limited to source reservoir pressures below 0.5 Torr and above 0.05 Torr.]

(ii) For many collisions, the random-walk formula can be applied, and gives the Gaussian distribution of angles [50]:

$$G(\theta)=\frac{2\theta}{\langle\theta^2\rangle}\exp\left(\frac{-\theta^2}{\langle\theta^2\rangle}\right),$$

$$\langle\theta^2\rangle=n\ell\int_0^\pi \theta^2 I(\theta)2\pi\sin(\theta)d\theta,$$

and

$$\theta_{1/2}=1.665\sqrt{\langle\theta^2\rangle}. \qquad (A4)$$

$I(\theta)$ is the scattering differential cross section; ℓ is the path length of the atom through the gas of number density n.

(iii) For most atomic gases, the hard-sphere scattering cross section $I(\theta)=\sigma_t/4\pi$ (isotropic) in the center of mass can be applied, and gives

$$\langle\theta^2\rangle=(\pi^2-4)n\ell\sigma_t. \qquad (A5)$$

where σ_t is the total scattering cross section. Thus the angular broadening of the gas is independent of the type of gas collision, i.e., whether *a* or *b* with itself or *a* with *b*. In such a case, for the two gases *a* and *b* which are mixed, the full width at half maximum of the angular distribution of gas $a(=\theta^{a'}{}_{1/2})$, broadened by *b*, from its unmixed value of $\theta^{a}{}_{1/2}$ can be obtained simply as

$$\theta^{a'}_{1/2}=\left((\theta^a_{1/2})^2+(\theta^b_{1/2})^2\left[\frac{1/\lambda_{ab}}{1/\lambda_a+1/\lambda_{ab}}\right]\right)^{1/2} \qquad (A6)$$

The broadening is considered in terms of the above random walk statistics with the factor in parenthesis being the weighted fraction of collisions between *a* and *b* as compared to *a* with itself and λ_{ab} is computed using Eq. (A7) with $\delta_{ab}=(\delta_a+\delta_b)/2$. Note that in the case when $\lambda_a \ll \lambda_{ab}$, $\theta^{a'}{}_{1/2}=\theta^a{}_{1/2}$ and the influence of inter-*a* and *b* collisions is negligible. On the other hand, if $\lambda_a \gg \lambda_{ab}$, the resultant value of $\theta^{a'}{}_{1/2}$ becomes a convoluted statistical sum of $\theta^a{}_{1/2}$ and $\theta^a{}_{1/2}$ in quadrature.

In this hard-sphere model, both *a* and *b* will experience broadening due to collisions with each other. The results of this model are shown in Fig. 18 for Ne mixed with He and for Ne mixed with H. The molecular diameter of H is not available in the literature, so we used $\delta=2a_0$ ($a_0=1$ Bohr radius) for H. The model largely confirms our experimental observations that, in a mixture of gases, the profiles of the constituents are very similar. However, atomic collisions are better represented introducing some forward-scattering, soft-sphere type collisions due to van der Waal type long-range Coulomb interactions [50]. The contribution of these interactions is to modify the hard-sphere collision isotropy and introduce deviations in the profiles of the constituents in the mixture. However, for the light atomic gases represented here, the soft-sphere behavior can be neglected and the profiles should be the same.

---

[1] M. A. Khakoo, C. E. Beckmann, S. Trajmar, and G. Csanak, J. Phys. B **27**, 3159 (1994).

[2] R. D. Cowan, *Theory of Atomic Spectra* (University of California Press, Berkeley, CA, 1981).

[3] X. Guo, M. A. Khakoo, D. J. Mathews, G. Mikaelian, A. Crowe, I. Kanik, S. Trajmar, V. Zeman, K. Bartschat, and C. J. Fontes, J. Phys. B **33**, 1895 (2000).

[4] M. A. Khakoo, S. Trajmar, L. LeClair, I. Kanik, C. J. Fontes, R. E. H. Clark, and J. R. Abdallah, Jr., J. Phys. B **29**, 3455 (1996).

[5] F. H. Nicholl and C. B. O. Mohr, Proc. R. Soc. London, Ser. A **142**, 647 (1933).

[6] W. C. Tam and C. E. Brion, J. Electron Spectrosc. Relat. Phenom. **2**, 111 (1973).

[7] D. Roy and J. D. Carette, Can. J. Phys. **52**, 1178 (1974).

[8] D. F. Register, S. Trajmar, G. Steffensen, and D. C. Cartwright, Phys. Rev. A **29**, 1793 (1984).

[9] M. A. Khakoo and J. W. McConkey, Phys. Rev. Lett. **57**, 679 (1986); J. Phys. B **20**, 5541 (1987); J. J. Corr, P. J. M. van der Burgt, P. Plessis, M. A. Khakoo, P. Hammond, and J. W. McConkey, J. Phys. B **24**, 1069 (1991).

[10] D. H. Madison, G. Csanak, and D. C. Cartwright, J. Phys. B **19**, 3361 (1986).

[11] L. Machado, E. P. Leal, and G. Csanak, J. Phys. B **15**, 1773 (1982).

[12] V. Zeman, K. Bartschat, T. J. Gay, and K. W. Trantham, Phys. Rev. Lett. **79**, 1825 (1997).

[13] K. A. Berrington, W. Eissner, and P. H. Norrington, Comput. Phys. Commun. **92**, 290 (1995).

[14] S. Fischer, G. F. Hanne, K. Bartschat, V. Zeman, and R. Srivastava, J. Phys. B **32**, 4447 (1999).

[15] V. Zeman and K. Bartschat, J. Phys. B **30**, 4609 (1997).

[16] T. Zuo, R. P. McEachran, and A. D. Stauffer, J. Phys. B **24**, 2853 (1991).

[17] I. Kanik, J. M. Ajello, and G. K. James, J. Phys. B **29**, 2355 (1996).

[18] M. J. Brunger, Ph.D. thesis, Dept. of Physics, The Flinders University of S. Australia, SA 5042, 1988.
[19] K. Bartschat and D. H. Madison, J. Phys. B **25**, 4619 (1992).
[20] X. Guo, M. A. Khakoo, D. J. Mathews, G. Mikaelian, A. Crowe, I. Kanik, S. Trajmar, V. Zeman, K. Bartschat, and C. J. Fontes, J. Phys. B **33**, L155 (1999).
[21] K. Bartschat and A. N. Grum-Grzhimailo, J. Phys. B **33**, 4603 (2000).
[22] M. A. Khakoo, M. Larsen, B. Paolini, X. Guo, I. Bray, A. Stelbovics, I. Kanik, S. Trajmar, and G. K. James, Phys. Rev. A **62**, 12701 (1999).
[23] J. H. Brunt, G. C. King, and F. H. Read, J. Phys. B **10**, 1289 (1977).
[24] B. P. Paolini and M. A. Khakoo, Rev. Sci. Instrum. **69**, 3121 (1998).
[25] I. Bray and A. Stelbovics, Phys. Rev. A **46**, 6995 (1992).
[26] D. F. Register and S. Trajmar, Phys. Rev. A **29**, 1785 (1984).
[27] M. A. Khakoo, T. Jayaweera, S. Wang, and S. Trajmar, J. Phys. B **26**, 4845 (1993).
[28] J. C. Nickel, P. W. Zetner, G. Shen, and S. Trajmar, J. Phys. E **22**, 730 (1989).
[29] R. I. Hall, G. Joyez, J. Mazeau, J. Reinhardt, and C. Schermann, J. Phys. (France) **34**, 827 (1973).
[30] S. Trajmar, D. F. Register, D. C. Cartwright, and G. Csanak, J. Phys. B **25**, 4889 (1992); D. C. Cartwright, G. Csanak, S. Trajmar, and D. F. Register, Phys. Rev. A **45**, 1602 (1992).
[31] J. F. Williams and A. Crowe, J. Phys. B **8**, 2233 (1975).
[32] C. E. Moore, *Atomic Energy Levels*, Natl. Bur. Stand. Circ. No. 467 (US GPO, Washington D.C., 1952).
[33] V. Zeman and K. Bartschat, J. Phys. B **30**, 4609 (1997).
[34] K. A. Berrington, W. B. Eissner, and P. H. Norrington, Comput. Phys. Commun. **92**, 290 (1995).
[35] D. H. Madison and W. N. Shelton, Phys. Rev. A **7**, 499 (1973).
[36] K. Bartschat and D. H. Madison, J. Phys. B **20**, 5839 (1987).
[37] C. Froese-Fischer, Comput. Phys. Commun. **4**, 107 (1972).
[38] F. A. Parpia, C. Froese-Fischer, and I. P. Grant, Comput. Phys. Commun. **94**, 249 (1996).
[39] W. F. Chan, G. Cooper, X. Guo, and C. E. Brion, Phys. Rev. A **45**, 1420 (1992).
[40] E. N. Lassettre and A. Skerbele, *Methods of Experimental Physics*, edited by D. Williams (Academic, New York, 1974), Vol. 3B, p. 868.
[41] L. Vriens, Phys. Rev. **160**, 100 (1967).
[42] S. Tsurubuchi, K. Watanabe, and T. Arikawa, J. Phys. Soc. Jpn. **59**, 497 (1990).
[43] Y. M. Alexandrov, P. F. Gruzdev, M. G. Kozlov, A. V. Loginov, V. N. Makhov, R. V. Fedorchuk, and M. N. Yakimenko, Opt. Spektrosk. **54**, 7 (1983) [Opt. Spectrosc. **54**, 4 (1983)].
[44] W. B. Westerveld, Th. F. A. Mulder, and J. Van Eck, J. Quant. Spectrosc. Radiat. Transf. **21**, 533 (1979).
[45] N. D. Bhaskar and A. Lurio, Phys. Rev. A **13**, 1484 (1976).
[46] T. Zuo, R. P. McEachran, and A. D. Stauffer, J. Phys. B **25**, 3393 (1992).
[47] F. Rugamas, D. Roundy, G. Mikaelian, G. Vitug, M. Rudner, J. Shih, D. Smith, J. Segura, and M. A. Khakoo, Meas. Sci. Technol. **11**, 1750 (2000).
[48] S. Dushman, *Vacuum Technique* (Wiley, New York, 1949).
[49] D. R. Olander and V. R. Kruger, J. Appl. Phys. **41**, 4641 (1970).
[50] G. A. Bird, *Molecular Dynamics and the Direct Simulation of Gas Flows* (Clarendon, Oxford, 1995).
[51] D. H. Madison, C. M. Maloney, and J. B. Wang, J. Phys. B **31**, 873 (1988).
[52] C. M. Maloney, J. L. Peacher, K. Bartschat, and D. H. Madison, Phys. Rev. A **61**, 022701 (2000).